A Study of Thickness Distribution and Crystal Structure of Sputter-deposited Silicon Thin Films

by

Farnaz Rashidi

B.Sc., University of Tehran, 2009

Thesis Submitted in Partial Fulfillment of the
Requirements for the Degree of
Master of Science

in the
Department of Physics
Faculty of Science

SIMON FRASER UNIVERSITY

Spring 2015

Approval

Name: **Farnaz Rashidi**

Degree: **Master of Science**

Title: ***A Study of Thickness Distribution and Crystal Structure of Sputter-deposited Silicon Thin Films***

Examining Committee: **Chair:** Eldon Emberly
Associate Professor

Dr. Erol Girt
Senior Supervisor
Associate Professor

Dr. David Broun
Supervisor
Associate Professor

Dr. Karen Kavanagh
Supervisor
Professor

Dr. Malcolm Kennett
Internal Examiner
Associate Professor

Date Defended/Approved: January 22, 2015

Partial Copyright Licence

Abstract

Silicon thin films have a wide range of applications in different industries such as microelectronics and solar cells. Controlling the properties of the film such as thickness, uniformity and crystal structure during the deposition process is of crucial importance in the final performance of the device. In this work, the thickness distribution and crystal structure of silicon films deposited by the magnetron sputtering technique were studied. A computer model was developed to simulate the thickness distribution of sputter-deposited silicon films. The simulation results were compared to the measured film thickness profiles obtained by X-ray reflectometry measurements. The good agreement between the experimental and simulation results demonstrates that the model is consistent with the observed experimental results. The crystal structure of silicon films were examined by means of the X-ray diffraction measurements. Silicon has an as-deposited amorphous structure. To induce the crystallization at low temperatures, a copper layer was deposited on top of the silicon film. The crystallization of silicon was observed at 340°C which is considerably lower than the solid phase crystallization of amorphous silicon (~700°C). It is also shown that silicon crystallites tend to grow in the [111] direction. The full width at half maximum of the silicon (111) peak is less than 2 degrees which indicates a strong texture along this direction.

Acknowledgments

I would like to thank several groups of people who helped me accomplish this thesis. First, to my supervisor, Dr. Erol Girt, who supported me through my study at Simon Fraser University from the first day and gave me motivation whenever I needed it the most. It was a pleasure to work with him.

I also thank Dr. David Broun and Dr. Karen Kavanagh for being on my supervisory committee and giving me guidance through my thesis. I thank Dr. Malcolm Kennett for agreeing to act as examiner.

I would like to thank the administrative staff of the Physics Department at SFU, specifically Jen Chang, Rose Evans, Stephen Flach, Ayako Nagasawa, and Joan Cookson for answering my so many questions patiently and helping me taking care of the paperwork.

I would like to thank all the people in our lab, specifically Ken Myrtle. Through my Master's project, I constantly benefitted from Ken's knowledge and I would like to thank him for teaching me so many things. I would like to thank Monika, Eric, Wendell, Nicholas, Bobo, and Tommy for helping me with various parts of this thesis and being such great colleagues.

During my study at SFU my life was made enjoyable by a number of friends who also kept me sane during the hard period of writing the thesis. I extend a very warm thank you to Laleh, Shima, Payam and Pooneh for being there for me whenever I needed them.

No amount of thanks is enough for three people. They are my parents and my younger brother without whom I would not be the person I am today. I would like to acknowledge my mother for her love, encouragements and sacrifices that made it possible for me to reach this milestone. I dedicate this thesis to my mother.

Table of Contents

Approval ii
Partial Copyright Licence iii
Abstract iv
Acknowledgments v
Table of Contents vi
List of Tables viii
List of Figures ix

Chapter 1. Introduction 1

1.1 Motivation 1

1.2 Thesis Organization 3

References 5

Chapter 2. Basic Concepts of Sputtering. 6

2.1 Principles of Sputtering (DC Discharge) 6

2.2 Radio Frequency Sputtering 13

2.3 Magnetron Sputtering 18

References 20

Chapter 3. Computer Simulation of Film Thickness Distribution in Magnetron Sputtering 21

3.1 Model 22

3.1.1 Receiving Flux at the Substrate 25

3.1.2 Angular Distribution of Sputtered Atoms 27

3.2 Experimental Procedure 32

3.2.1 Sample Deposition 32

3.2.2 Thickness Measurements 34

3.3 Results and Discussion.....37

3.4 Conclusion.....43

References.....45

Chapter 4. Enhancing the Crystallization and Texture of Silicon Films using a Copper Seed Layer.....48

4.1 Metal Induced Crystallization (MIC).....50

4.2 Experimental Procedure..... 53

4.2.1 Sample Deposition.....53

4.2.2 Structural Characterization.....55

4.3 Results.....56

4.4 Discussion.....60

4.5 Conclusion.....66

References.....67

Chapter 5. Conclusion.....71

List of Tables

Table 4.1 The crystallization activation energy of a-Si/metal bilayers under thermal annealing.....52

Table 4.2. Si and Cu_3Si diffraction peak positions and corresponding (hkl) planes 59

Table 4.3. Atomic structure and physical properties of copper and silicon.....61

List of Figures

Figure 2.1. A typical setup of DC sputtering discharge. 7

Figure 2.2. Plot of the break down voltage versus pressure and electrodes spacing 8

Figure 2.3. The electric potential of a DC discharge 10

Figure 2.4. Ion-target interactions 12

Figure 2.5. Formation of negative DC bias on capacitively coupled cathode in an RF discharge 14

Figure 2.6. The electric potential profile of target and plasma 15

Figure 2.7. The time-averaged potential distribution in an RF discharge 16

Figure 2.8. E-field and B-field lines configuration in magnetron sputtering. 18

Figure 3.1. The off-axis source-substrate configuration in the circular magnetron sputtering system 23

Figure 3.2. The source-substrate configuration 25

Figure 3.3. Different types of angular distribution 30

Figure 3.4. Yamamura's angular distribution function 31

Figure 3.5. Different source-substrate configurations. 33

Figure 3.6. The X-ray reflectivity curve from a silicon film 35

Figure 3.7. The optical paths of X-rays reflected from the top and bottom surface in a single component film 36

Figure 3.8. Simulated and measured film thickness profiles for the first set of samples at different source-substrate positions 38

Figure 3.9. Simulated and measured film thickness profiles for the second set of samples at different source-substrate positions 39

Figure 4.1. The summary of the influence of a metal film on the crystallization temperature of a-Si. 49

Figure 4.2. The structure of the samples prepared for the experiment 54

Figure 4.3. The X-ray Diffraction set up 55

Figure 4.4. The XRD pattern of Ta/Si stack annealed to 480℃. 56

Figure 4.5. The XRD patterns for Ta/Cu/Si stack 57

Figure 4.6. The stacking structure of Cu fcc lattice 58
Figure 4.7. Unit cell structures of Cu3Si and Si crystals from the ICSD. 59
Figure 4.8. Omega scan of the silicon (111) peak 60
Figure 4.9. Cu–Si phase diagram 63
Figure 4.10. The atomic arrangements in the crystallographic planes. 64

Chapter 1

Introduction

1.1 Motivation

A thin film is a layer of a substance that is applied on a supporting material called a substrate. The process of applying the thin film on the substrate is called thin film deposition. While “thin” is a relative term, in thin film industries it covers thicknesses from a few nanometers to several microns. Thin films have a vast range of applications from the coatings on the household mirrors to the sensors of the space shuttle components.

There are several techniques available to deposit the thin films. In general, the techniques fall into two categories of chemical and physical deposition depending on the nature of the processes involved. Examples of chemical deposition include chemical vapour deposition (CVD), atomic layer deposition (ALD) and chemical solution deposition (sol-gel processing). Thermal evaporation, pulsed laser deposition (PLD), and sputtering are examples of physical deposition methods. Each of these methods has its benefits and disadvantages and can be used based on the process requirements and conditions. Among the abovementioned techniques, sputtering is one of the most widely used methods in industry for thin film depositions. It offers a relatively good control over the film properties such as uniformity, thickness, crystal structure and composition. These properties are very important in determining the quality of the thin films.

The aim of this thesis is to study the fundamental concepts of the sputtering process and to investigate the thickness distribution and crystal structure of the sputter-deposited

films. I chose silicon as the material to be deposited since it has been extensively studied and it has a wide range of applications.

This thesis can be divided into three parts: 1. In the first part, the basic concepts of the sputtering technique are reviewed. 2. The second part deals with the thickness distribution of the sputter-deposited silicon films. 3. In the third part, the crystallization behaviour of silicon films induced by a copper seed layer is investigated.

All the samples studied in this thesis were deposited by using the RF/DC magnetron sputtering system. The history of sputtering goes back to over one hundred years ago when electricity was applied between the two electrodes placed at the ends of a low pressure gas container. In the presence of the electric field, the ionized gas molecules accelerate toward the cathode electrode. Under the bombardment of energetic particles atoms are knocked out of the cathode. This phenomenon is called sputtering. When the liberated atoms condense on a substrate, the process is called sputter deposition.

The sputtering technique was used as early as 1877 to coat mirrors [1-1]. However, it wasn't until a few decades ago that the application of sputtering for thin film deposition received considerable attention. By the introduction of radio frequency (RF) and magnetron sputtering as well as improving the vacuum systems, impurity of the targets and working gas sputtering has become a very demanding technique for film deposition. RF sputtering has made it possible to deposit almost any material irrespective of its conductivity and magnetron sputtering has considerably increased the deposition rates by including magnets/magnetic coils into the design of the system. Some of the advantages to film deposition using the sputtering technique include [1-1]:

1. High deposition rates (with magnetron sputtering)
2. Low temperature deposition
3. Scalability to large areas
4. Good control over the film composition and microstructure
5. Versatility to deposit alloys and compounds of various type and different vapour pressure
6. Good adhesion to the substrate

7. Employing a reactive gas as the sputtering medium to deposit compounds from elemental targets.

1.2 Thesis Organization

Chapter 2: Since sputtering is an important part of this thesis, chapter 2 is dedicated to overview the basic physics of sputtering to the extent which is necessary to understand the results of this thesis. Three variants of sputtering including the direct current (DC), RF and magnetron sputtering are discussed. Special attention has been paid to the electric potential distribution in the RF and DC discharges as it determines the energy of the bombarding ions. The results of this chapter have been used in Chapter 3.

Chapter 3: This chapter deals with simulating the film thickness distribution. A theoretical model is presented to predict the thickness distribution of the deposited films. The film thickness distribution is a function of multiple variables such as the system geometry, bombarding ions energy and their angular distribution. A computer program was developed to conduct the numerical calculations and simulate the thickness uniformities.

Film thickness uniformity is of major importance in many of the sputtering applications. Many theoretical models have been proposed to determine the optimum geometry that results in a uniform film deposition. Since the sputtering systems are very different in terms of the geometry and employed sputtering parameters, the applicability of the proposed models to different sputtering systems are not very straightforward.

The conditions and assumptions that were considered in developing the model are specific to the sputtering system that I used to fabricate the samples. To verify the model, several samples were deposited at different target-substrate geometries and their thicknesses were measured by means of the X-ray reflectometry measurements. The simulation and experimental results are compared and presented.

Chapter 4: In this chapter, the metal-induced crystallization (MIC) of silicon is discussed and the effect of copper on the crystallization temperature of a sputter-deposited silicon film has been studied. Silicon has an as-deposited amorphous structure and it

crystallizes by annealing to high temperatures (≥700℃); however, studies show that Si crystallization temperature considerably drops to lower temperatures when Si is in contact with a metal layer. MIC is a relatively low cost and low temperature method to obtain polycrystalline silicon compared to other techniques such as CVD, laser annealing, solid phase crystallization, etc.

Multiple samples composed of a bilayer of silicon-copper film were deposited on glass substrates and each one was annealed to a different temperature (340℃ -480℃). The microstructural behaviour of the samples was examined by X-ray diffraction measurements and it was shown that the crystallization temperature of amorphous silicon in contact with copper is reduced.

Chapter 5: Finally, in chapter 5, a summary of the obtained results will be presented.

References

[1-1] Joy George, *Preparation of Thin Films*, CRC Press, 1992

Chapter 2

Basic Concepts of Sputtering

Introduction

In this chapter a brief description on the physics of sputtering will be given and the principles of DC, RF and magnetron sputtering will be discussed.

2.1 Principles of Sputtering (DC Discharge)

Sputtering is a process through which atoms are ejected physically from a solid target upon the bombardment of the target by energetic particles. These energetic particles are generally ionized particles of a sputtering gas like argon. Argon is an ideal sputtering medium since it's a noble gas that doesn't react with the target material. The process begins when a stray electron accelerates in the electric potential that is established between the target (cathode) and substrate (anode). The electron collides with a neutral gas atom and converts it to a positively charged particle:

$$Ar + \bar{e} \longrightarrow Ar^{+} + 2\bar{e} \qquad (2.1)$$

The ionization potential of argon is about 15.76 *eV*. The charged particles, in this case Ar^{+}, then gain kinetic energy in the presence of the electric field and accelerate toward

the cathode target. Upon collision of energetic ions on the target, atoms are ejected from the target and are deposited onto the anode substrate.

Depending on energy of the ions and the target material, secondary electrons can also be liberated from the target surface upon impingement of ions on the target. These secondary electrons along with the electrons produced from the ionization (Equation 2.1) re-gain energy in the electric potential and collide with more neutral gas atoms and generate a cascading process that results in a gas break down and formation of plasma. Continuous production of electrons from both mechanisms is required to sustain the plasma. It should be noted that not all the collisions between electrons and argon neutrals result in the ionization of argon atoms. If electron energies are less than the ionization energy, the argon atoms can still be excited. The excited argon atoms go back to their ground states creating the glow of the plasma.

Figure 2.1 shows a typical setup of a direct current (DC) sputtering system and the collision processes in the discharge.

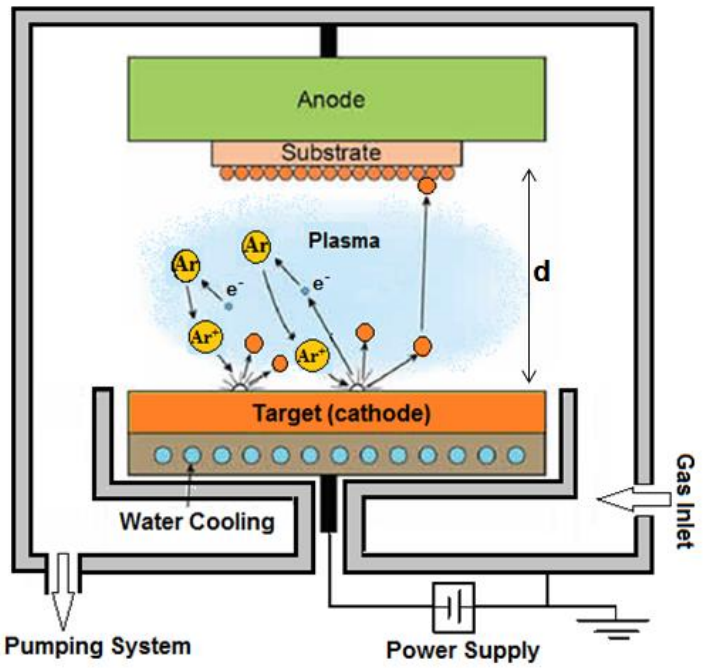

Figure 2.1: A typical setup of DC sputtering discharge. The target acts as cathode and is connected to the cooling system. The substrate and walls are grounded. In this configuration the electrodes are parallel and separated by distance d.

To initiate the discharge, the vacuum chamber is evacuated to a base pressure of approximately 10^{-7} *torr*. The low base pressure is required to keep the impurity concentration to a minimum in the deposited film. Once the base pressure has reached a satisfactory level, the sputtering gas (argon in our case) is introduced into the chamber. The initial pressure of argon inside the chamber is adjusted so that there will be enough gas molecules to ionize. At this point, a negative potential of a few hundred volts is applied to the cathode substrate while the anode target and chamber walls are grounded. By applying an electric field on the gas sample, plasma will be produced once an avalanche-like ionization process begins. The voltage at which gas breakdown occurs is described by Paschen's law [2-1]. For a particular gas and target material, the breakdown voltage (V_B) was found to depend on the product of the pressure (P) in the chamber and electrode separation (d). Figure 2.2 qualitatively shows the behaviour of V_B in terms of P and d. Plots of V_B versus Pd are known as Paschen curves.

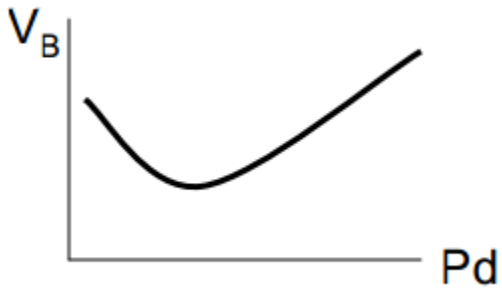

Figure 2.2: Plot of the break down voltage versus pressure times electrodes spacing.

At too high pressures and/or large electrode separation distances, electrons undergo so many collisions that they do not have enough time to gain sufficient energy to ionize the gas atoms. On the other hand, when the pressure is too low and/or anode-cathode separation is small, there are not enough collisions between electrons and atoms to sustain the discharge. So for both extreme ends of horizontal axis in Fig.2.2, a higher voltage is required to generate enough energetic electrons to breakdown the gas. The characteristic minimum is reached at some intermediate value of Pd.

It should be noted that Paschen curves for different gases and target materials have the same shape but different V_B values.

After the plasma is ignited, the argon pressure is reduced to the minimum level at which the plasma can be self-sustained, since film depositions are preferred to be conducted at low pressures. The typical working pressure of the sputtering gas is around several militorrs. Collisions between the sputtered atoms and background gas change the direction and reduce the energy of the sputtered atoms. The change in the direction causes the sputtered atoms to be deposited on the chamber walls rather than the substrate, so the deposition rate decreases. The reduction in their energy results in a rough film as sputtered atoms do not have enough energy to diffuse along the substrate surface to find the lowest energy position. Thus to obtain higher deposition rates and smooth films, the working pressure of the sputtering gas should be kept as low as possible.

Plasma Diagnostics: Electric Potential and Species Energy

Plasma is a partially ionized gas composed of ions, electrons and neutrals that is electrically quasi-neutral ($n_i \sim n_e$). The plasma that forms during the sputtering process is called the glow discharge. The most energetic particles in the glow discharge are electrons. Measurements on glow discharges have shown that the average electron energies are in the range of 1-10 *eV*. Neutrals and ions are not as energetic as electrons and their energies are less than 0.1 *eV*, however, ions on average are more energetic than neutrals since they can gain energy from the applied electric field [2-2]. The energy of the species is determined by collision frequencies, the collision mechanism, as well as the applied electric potential. Figure 2.3 shows a typical steady-state electric potential distribution in a DC sputtering discharge. Three major regions that can be distinguished in the discharge are: the cathode sheath, the glow region (bulk plasma), and the anode sheath. The sheaths are positively charged regions that are formed adjacent to the electrodes and separate the plasma body from the anode and the cathode.

The basic principles leading to the formation of plasma sheaths can be understood by considering the situation where the plasma is confined between two isolated (grounded) electrodes. Immediately after the plasma comes into contact with the electrodes, the fast-moving electrons will drain to the walls leading to the formation of a net positive space charge region near the electrode walls due to the presence of more inert positive ions.

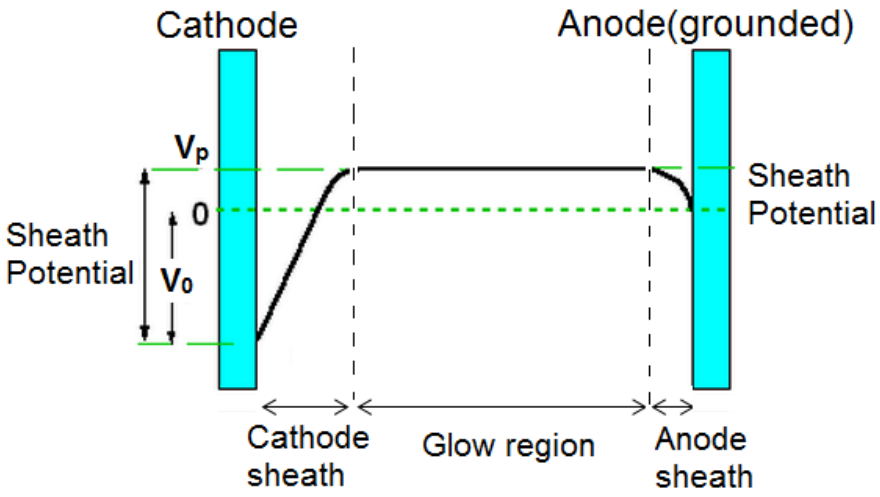

Figure 2.3: The electric potential of a DC discharge.

Therefore, an electric field will be established over the positive space charge region that prevents the net flux of electrons to the walls. The electric field leads to a potential profile with a positive value within the plasma and rapidly drops to zero over the space charge regions adjacent to each electrode. The typical values of the plasma potential (V_p) are around 5-10*V* which is necessary to confine most of the electrons within the bulk plasma. The thickness of the sheaths at the grounded electrodes is of the order of the electron Debye length (~ 0.01 *mm*) [2-2].

The case of the plasma confined between two grounded electrodes is different from the situation where the cathode target has a large negative voltage (usually 100-1000*V*). In this case the electric potential profile is similar to what is shown in Fig.2.3.

The cathode sheath: most of the discharge voltage is carried over the cathode sheath. The increased potential between the plasma and cathode will increase the sheath thickness and depending on the applied DC voltage, the thickness can reach a few millimetres. Positive ions that enter this area from the bulk plasma accelerate toward the cathode and bombard it with high energies. In a DC discharge, the sheath voltage is the difference between the plasma potential (V_p) and cathode voltage (V_0) and since V_0 is much larger than V_p, the cathode sheath voltage is usually approximated with V_0 which is constant. The maximum energy that ions can gain before striking the cathode is then

equal to eV_0. However due to the collisions of ions with the background gas, they do not gain the maximum energy but end up with some energy distribution. The cathode sheath is also called cathode dark space because the secondary electrons that are emitted from the target do not have enough energy to excite or ionize any gas particles [2-4].

The bulk plasma: the glow region is the quasi-neutral bulk plasma with a slightly elevated potential (5-10*V*) with respect to the anode (grounded electrode). The electric potential is nearly constant across the bulk plasma. The luminous glow is produced because electrons have gained sufficient energy to excite the sputtering gas atoms.

The anode sheath: the region that potential drops from V_p to zero on the anode is called the anode sheath. Just like the cathode side, positive ions that enter this region are accelerated toward the substrate; however the potential drop across this region is too small to give ions enough energy to sputter material from the substrate. The required energy to sputter atoms from the target depends on the target material and its surface binding energy. For silicon, the threshold energy of sputtering by normally incident argon ions is about 30 *eV*. [2-3]

The electric potential profile that was discussed here is typical to most DC discharge sputtering systems. However, the width and number of distinguishable regions within the discharge can vary as the pressure and/or cathode-anode spacing changes [2-2]. The study of discharge potentials with more distinguishable regions is beyond the scope of this thesis.

Ion-target Interactions

The energy of the ions incident on a substrate is determined primarily by the cathode sheath potential. Upon collision of an ion on the target, its energy and momentum are transferred to the target atoms. For the most efficient energy transfer, the ions should have the same atomic mass as the atoms of the target materials. Argon matches relatively well with a wide range of materials that are mostly used for sputter deposition. The interaction between the bombarding ions and target material depends on the energy of the ions, angle of incidence, and the bonding energy of the target material.

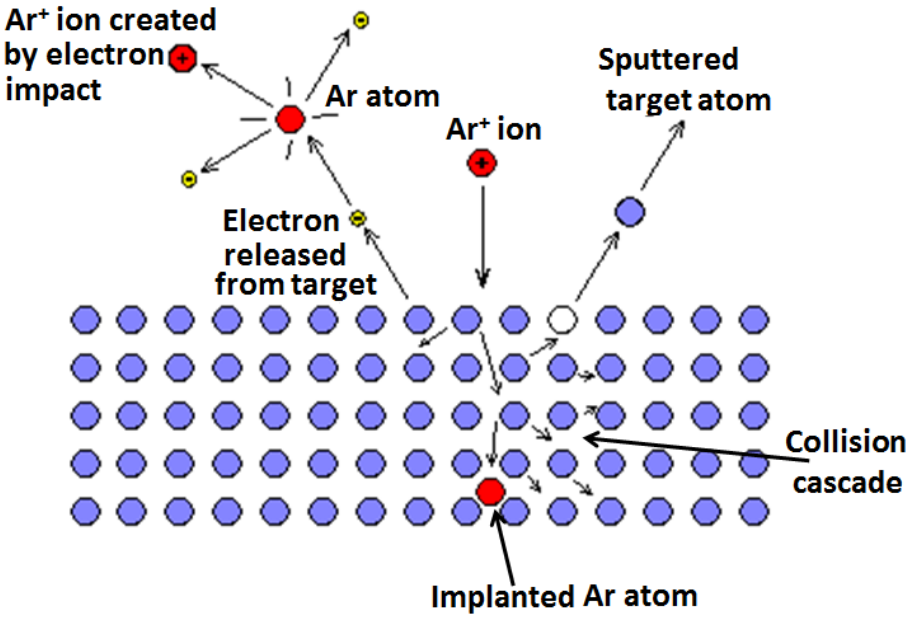

Figure 2.4: Ion-target interactions [2-5]

Figure 2.4 depicts some of the processes that happen when the target surface is hit by an ion [2-5]. Upon collision of ions on the cathode, several events can occur:

- The ion can be reflected from the target surface or neutralized by the electrons emitted from the target.
- The ion bombardment can knock an electron out from the surface (secondary electron).
- The ions can penetrate into the target (ion implantation).
- Finally the impact of ions can generate a series of collisions, known as the collision cascade, within the target material that leads to the ejection of target atoms and sputtering.

The latter is discussed in more detail in Chapter 3. The majority of species ejected from the target material are neutrals; however, electrons, adsorbed gases and ions can be emitted from the target surface as well. These unwanted particles can hit the substrate along with the target atoms and affect the quality of the film.

2.2 Radio Frequency Sputtering

One of the limitations of DC sputtering is that the target needs to be electrically conductive. Using an insulating target in DC sputtering causes a charge buildup during the ion bombardment so the target blocks the DC current and no stable gas discharge can be created. Sputtering from a dielectric or an electrically insulating target can be carried out by using an alternating or radio frequency (AC or RF) power supply.

In a typical RF sputtering system, the target is powered by an RF generator while the substrate is grounded. For this section of the thesis, the terms cathode and anode will be used interchangeably for target and substrate respectively. The voltage applied to the cathode oscillates between a negative cycle to attract Ar^+ ions and a positive cycle to attract electrons that neutralize the positive charge buildup. The key factor which allows RF sputtering is the large mass difference between the ions and the electrons.

For a typical laboratory sputtering system with the applied voltage of a few hundred volts, at frequencies below 0.5 *MHz*, both ions and electrons are mobile and can follow the voltage and oscillate back and forth but in opposite directions. It can be viewed as DC sputtering of both target and substrate that alternatively behave as cathodes and anodes. At frequencies above 0.5 *MHz*, ions are too heavy to follow the voltage and they move much less compared to the dimensions of the plasma sheaths. In contrast, electrons would easily follow the variations of applied electric field and they can gain enough energy to cause ionization. It is important to note that, the 0.5 *MHz* cut-off frequency depends on the ion's mass, applied voltage, system dimensions and sheath thicknesses. Since ions cannot respond to the applied electric field at high frequencies, they are not able to accelerate toward the target during its negative cycles and gain enough energy to sputter target material. However, if the target is a dielectric, it acts as a capacitor in series with the plasma and self-biases itself to a negative potential. In this case, the ions can respond to this negative DC bias and accelerate toward the target.

The negative DC bias (V_{DC}) is a consequence of disparity in electrons and ions mobilities in the applied RF electric field. Initially, the target electrode draws more electron current during its positive cycle than it draws ions current during its negative cycle so the net average current over one full cycle is non-zero. However this cannot continue since the

target is an insulator and it does not allow the flow of a net electric current through. To make the net current zero, a negative self-bias establishes over the target. With the negative self-bias, the target has a negative voltage for most of the RF cycle so the ions flux during the longer negative cycle balances with the electrons flux during the shorter positive cycle, resulting in the net zero current over one full RF cycle. Figure 2.5 helps to explain the concept of self-bias at the powered electrode.

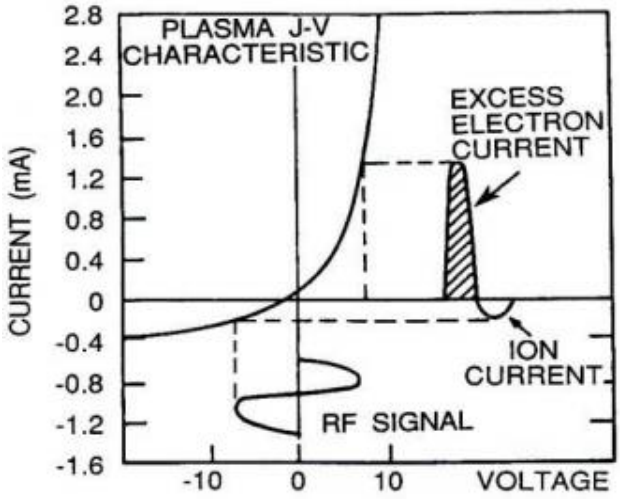

(a)

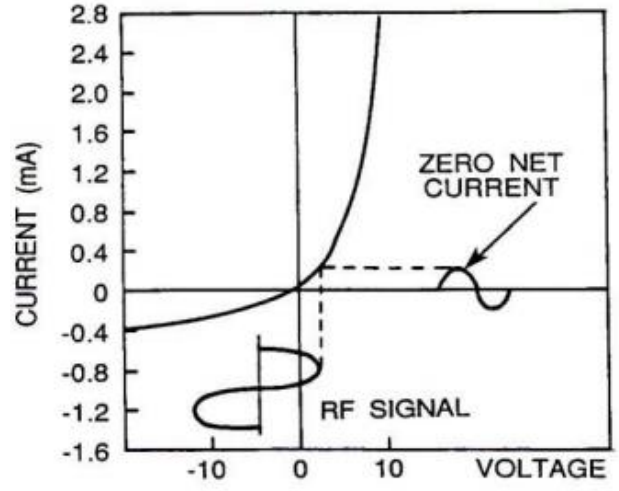

(b)

Figure 2.5: Formation of negative DC bias on capacitively coupled cathode in RF discharge (a) with net current and zero self-bias voltage (b) zero net current and negative self-bias voltage [2-2]

Since the target acts as a capacitor, its impedance is inversely proportional to the frequency. Therefore, at frequencies above 1 *MHz*, the RF voltages can be coupled through almost any impedance and any material can be sputtered irrespective of its resistivity. Commercial RF sputtering systems are generally operated at 13.56 *MHz*. In addition to sputtering insulating materials, one of the main advantages of RF sputtering over DC sputtering is that electrons oscillating in an RF field couple energy more efficiently to the plasma. This leads to higher ionization rates without requiring the secondary electrons from the target to sustain the plasma. The plasma in an RF discharge can then be sustained at lower pressures compared to a DC discharge [2-2].

Figure 2.6 shows the electric potential profile of the cathode (powered electrode) and plasma with respect to time. The plasma potential V_p is modulated with the RF voltage and it remains positive with respect to the zero potential (grounded electrode potential). Clearly the magnitude of the DC self-bias depends on the amplitude of the RF signal. The value of V_{DC} also depends on frequency and electron densities [2-6].

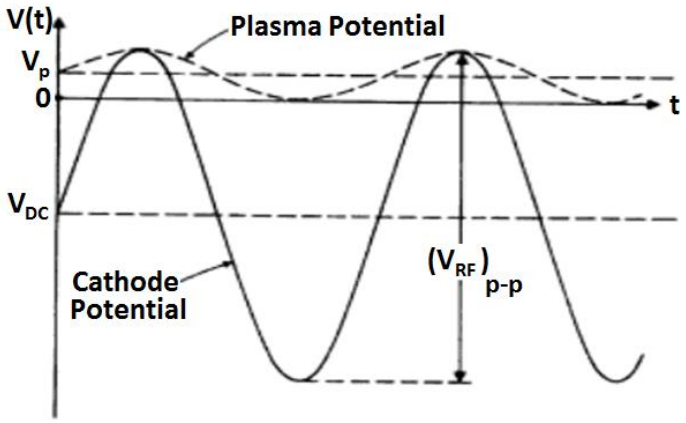

Figure 2.6: The electric potential profile of target and plasma [2-6]

Figure 2.7 shows the time-averaged electric potential in an RF discharge [2-6]. The potential profile is similar to the one for DC sputtering; however, the distribution shown in Fig. 2.7 is time-averaged over one RF cycle. The electric sheaths are formed adjacent to the electrodes. The average cathode sheath potential is $|V_{DC}| + V_p$ and the average anode sheath voltage is V_p. The thicknesses of the cathode and anode sheaths

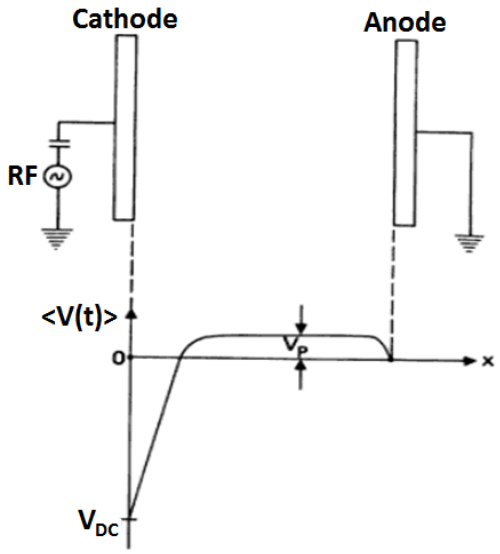

Figure 2.7: The time-averaged potential distribution in an RF discharge [2-6]

oscillate with the RF frequency and their averages depends on the pressure and applied power [2-6].

Positive argon ions from the plasma are accelerated over the cathode sheath region and gain enough energy to sputter atoms from the target. The maximum energy that the positive ions gain is

$$E_{max} = e\left(|V_{DC}| + V_p\right) = eV_t\,, \tag{2.2}$$

where V_t is the potential drop across the target sheath. On the other hand, the maximum energy that positive ions can gain over the anode sheath would be

$$E_{max} = eV_p = eV_s\,, \tag{2.3}$$

where V_s is the potential drop across the substrate sheath. Equations 2.2 and 2.3 can be deduced from Fig.2.7. The typical values of V_t and V_s in an RF discharge are about 300V and 20V respectively and it is clear that sputtering mainly occurs on the target.

So far, we assumed that the substrate is conductive and it is grounded. However, if the substrate is an insulator, there will be a negative DC bias buildup on the substrate as

well as the target. The negative DC bias on both cathode and anode leads to the sputtering of both surfaces. This problem can be solved by changing the relative geometry of target and substrate. When both target and substrate are capacitively biased, plasma potential drops significantly at both cathode and anode sheath regions. These regions can be modeled as capacitors and the equivalent circuit of the sputtering systems can be thought of as two capacitors in series, one at the target sheath region, and the other at the substrate, with the applied voltage divided between them. Since the capacitive reactance of a capacitor is inversely proportional to the capacitance or area, more voltage will be dropped across the capacitor with smaller surface area. It has been shown that the ratio of the voltages across the sheaths is given by the following expression:

$$\frac{V_t}{V_s} = \left(\frac{A_s}{A_t}\right)^n, \tag{2.4}$$

where A_s and A_t are the substrate and target electrode areas respectively and $2 \leq n \leq 4$ [2-6]. Hence if the area of the substrate is larger than that of the target, the potential drop across the substrate sheath would be very small and sputtering of the substrate will be minimized. In actual sputtering systems, the substrate and the entire chamber are grounded, making a very large electrode that leads to raising the target sheath potential while minimizing the ion bombardment of the grounded fixtures including the substrate. Since in the case of asymmetric electrodes, the plasma potential (V_p) is much smaller than the DC bias voltage (V_{DC}), the average potential that ions are accelerated through is approximated by the DC bias or from Equation 2.2: $V_t \sim V_{DC}$ This approximation was used to determine the energy of the bombarding ions in our experiment.

As discussed so far, RF sputtering enables sputtering from insulating targets. Nevertheless, it can be used to sputter conductive materials as well. In the case of a metal target, a blocking capacitor is placed in series with the target to establish the negative DC self-bias which is necessary in RF sputtering. With the capacitor, the DC current will not flow in the circuit and a negative bias is established on the metal electrode that accelerates the massive ions toward the target. Generally the blocking capacitor is built into the impedance-matching network which is placed between the RF power supply and discharge chamber. The matching network is necessary since the

plasma impedance is normally different from that of the RF power supply. The matching network maximizes the efficient power transfer from the power supply to the plasma.

2.3 Magnetron Sputtering

In order to enhance the confinement of the electrons near the target and increase the ionization efficiency, magnets are incorporated into the sputtering source. Figure 2.8 schematically shows the configuration of the magnets and field lines in a typical magnetron sputtering system. The electric field lines are perpendicular to the target and change direction in case of RF sputtering. The magnetic field lines first emanate normal to the target from the north magnetic pole, then bend with a component parallel to the target surface and finally return to the target, completing the magnetic circuit.

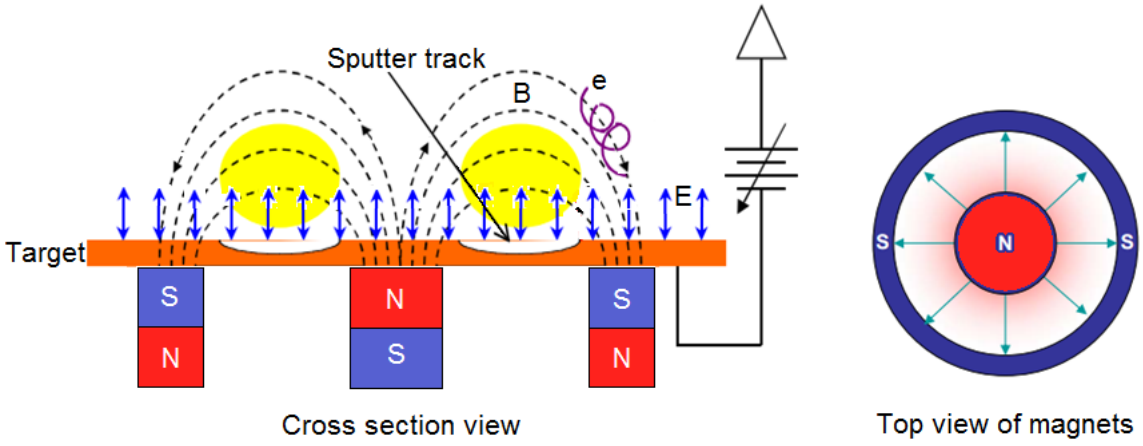

Figure 2.8: E-field and B-field lines configuration. Magnets below the target trap electrons in helical orbits around the magnetic field lines.

The electrons that are emitted from the target will be trapped by the magnetic field and move in helical orbits that end in the target surface. In our sputtering system, the magnetic fields are generated by permanent magnets made of NdFeB (Neodymium Iron Boron) alloy.

As it can be seen from the Fig.2.8, a sputtering track is formed on the target. Target erosion occurs within this track because the ionization density is most intense above this area. The shape of the erosion track depends on the magnetic field profile and strength.

The magnetic fields improve the ionization process in two ways; by increasing the probability of electrons striking an argon atom and by increasing the electron path lengths. Also, by confining the electrons near the target area, fewer of them reach the substrate. Due to the increase in ionization efficiency, magnetron sputtering can be carried out at lower pressures than for glow discharges without magnetic assistance and higher deposition rates can be obtained.

The strength of the magnetic field is adjusted in such a way that the electrons' Larmor radii ($\sim 10^{-3}\,m$) are small compared to the plasma size. The magnetic field strengths are usually on the order of 200 to 500 *Gauss* at the cathode surface where the B-field is tangent to the surface. The ions are not affected by the magnetic field since their Larmor radii ($\sim 10^{-1}\,m$) become very large compared to the dimension of the plasma. The exact range of magnetic field strength depends on the system geometry.

Magnetron sputtering works with both RF and DC power supplies and has been widely used for low pressure and low temperature sputtering. However, there are a few drawbacks to using this method. One of the main disadvantages of magnetron sputtering is that the uniformity of the deposited films is worse compared to cathodes without the magnetic confinement. The reason is that the non-uniform profile of the magnetic field leads to the non-uniform erosion of the target. So materials are mostly sputtered from the erosion track and not uniformly from the target surface. Consequently, typical target utilization values for magnetron sputtering are small and in the range of 10-25%. By changing the configuration of the magnets, the utilization rate can be adjusted to higher values but it is still less than the utilization rate in conventional sputtering where most of the target area is sputtered.

References:

[2-1] M. A. Lieberman, A. J. Lichtenberg, *Principles of Plasma Discharges and Materials Processing*, Wiley Interscience, New York, 1994, pp 8-10.

[2-2] Milton Ohring, *Materials Science of Thin Films*, Academic Press, USA, 1992.

[2-3] G. K. Wehner, Phys. Rev. 102, 690 (1956).

[2-4] John E. Mahan, *Physical Vapor Deposition of Thin Films*, John Wiley & Sons, New York, 2000.

[2-5] “Sputter Deposition”, Oxford Vacuum Science, accessed December 4, 2014. http://www.oxford-vacuum.com/background/thin_film/sputtering.htm .

[2-6] Mark J.Maou, *Fundamentals of Microfabrication: The Science of Miniaturization*, Second Edition, CRC Press, Florida, 2002.

Chapter 3

Computer Simulation of Film Thickness Distribution in Magnetron Sputtering

Introduction

Magnetron sputtering is a versatile technique to prepare thin films for a wide range of applications. Regarding the main film quality, the thickness uniformity is of crucial importance since it directly affects the physical properties of the film and thus the performance of the device. To make highly uniform films on large depositing areas and controlling the film thickness distribution have been the subject of investigation in many publications.

The thickness of the sputter-deposited film is primarily determined by the geometry of the target relative to the substrate. Other factors affecting the film thickness distribution are the discharge characteristics (power, pressure, etc.), the magnetron source, and the source-substrate relative motions [3-1]. In the past few decades numerous studies have been carried out on various types of sputtering systems to predict film thickness uniformities. However, since the film thickness distribution is a function of multiple variables, it is not possible to deduce a general, non-integral equation that describes the thickness distribution based on all the major factors [3-1]. Nevertheless, computer simulations and semi-empirical formulae have been developed based on analytical models to better explain the thickness distribution profiles.

Over the years, the simulation models have helped to modify the geometry of the target relative to the substrate to achieve higher uniformities. As an example, Swann *et al*. demonstrated that the off-axis magnetron source and a rotating workholder improve the film thickness uniformity compared to the conventional magnetron sources where the sputtering source shares the same axis of symmetry with the substrate [3-2]. The simulation models have also helped to re-design the magnetic field profile of the magnetron sources to yield the best target utilization for a specific source-substrate geometry.

In this chapter a theoretical model is proposed to predict the thickness distribution of a silicon film deposited by a Radio Frequency (RF) circular magnetron sputtering system. A computer program was developed in Mathematica (version 9.0) [3-3] to perform the numerical calculations and simulate the film thickness distribution. The model includes two fitting parameters that were calculated by fitting the experimental results to the simulations. The thickness of the films was measured using a grazing incidence X-ray reflectometry measurement.

The goal of this study is to verify the proposed model and thus determine the optimum geometry to obtain the desired uniformity over the depositing area. It is expected that the calculation method used in this work can be applied to other magnetron sputtering systems as well.

3.1 Model

In order to calculate the thickness distribution of a sputter-deposited film, one has to consider the arrangement of the target relative to the receiving surface. Figure 3.1 demonstrates the schematic view of the off-axis source-substrate configuration that was used in our experiment. The sputtering source is aligned at 17° oblique incidence onto the rotating substrate with a horizontal offset from the substrate center. The substrate is a circular disk whose central axis intersects the central axis of the target. The vertical and horizontal (offset) distances between the centers of the target and substrate are labelled as Z_0 and d respectively.

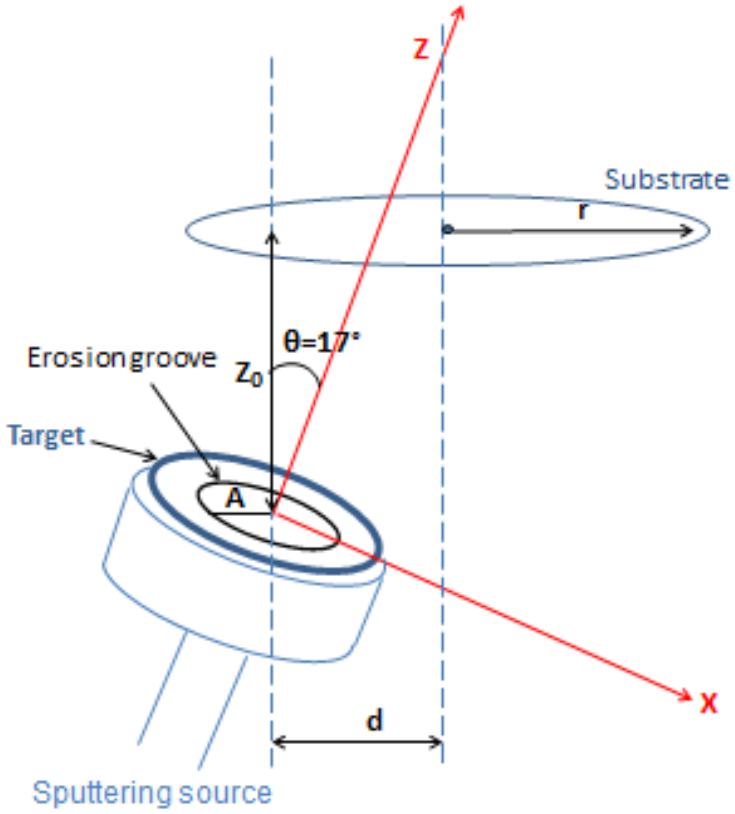

Figure 3.1: The off-axis source-substrate configuration in the circular magnetron sputtering system. The source is tilted by 17° with respect to the normal line to the substrate.

During the sputtering process, the target develops an erosion groove the shape of which depends on the magnetic field profile of the sputtering source. As the target is being utilized the erosion profile changes and it affects the film thickness distribution on the substrate. In our experiment, the shape of the erosion groove is a ring and its radius is labelled as A in Fig.3.1.

In this study, several assumptions have been made to simplify the model:

1. All the sputtered particles leave the target from the erosion ring. This ring is concentric with the target and has a constant radius. Since a new target was used for this experiment, I did not consider the width or depth profile for the ring.

2. I studied the case where the pressure is low enough so that the mean free path of the sputtered atoms becomes comparable to, or larger than, the source to substrate dimensions. Thus, the collisions between the sputtered atoms, argon atoms, and argon ions are neglected. As a result, the sputtered atoms travel along a straight line as they leave the target. In the case of Ar ion bombardment of a Si target, the mean free path (MFP) of the sputtered atoms is given by:

$$\lambda = \frac{1}{\pi(r_1 + r_2)^2 n}, \tag{3.1}$$

where r_1 and r_2 are the atomic radius of sputtered atoms and discharge gas particles respectively and n is the number density of discharge gas. At working pressure of 0.7 *mtorr* and room temperature, the MFP of sputtered silicon atoms is ~ 14 *cm* that is larger than source-substrate distances employed in our experiment.

3. It was assumed that the bombarding ions strike the target surface perpendicularly. The ions angle of incidence can be calculated from the following expression:

$$\theta_i = \frac{v_T}{v_N}, \tag{3.2}$$

where v_T and v_N are the tangent and normal components of the ions velocity on the target's surface. v_T is attributed to the thermal velocity of the ions and can be calculated from the ions' thermal energy (~ 0.1 *eV*). v_N is the velocity that ions gain when they are accelerated in the direction of cathode sheath electric field, normal to the target. Assuming a sheath potential of 100 *V*, ions gain a kinetic energy of 100 *eV* in the sheath and v_N can be calculated accordingly. By substituting the calculated v_N and v_T values from the corresponding kinetic energies, the ions angle of incidence is found to be less than 2°.

4. The diffusion, reflection and re-evaporation of the sputtered atoms on the surface of substrate were neglected.

The theoretical calculations in the following sections are based on the receiving flux at different positions on the substrate.

3.1.1 Receiving Flux on the Substrate

The thickness of a sputter deposited film is proportional to the receiving flux on the substrate. In this section the flux of particles was calculated for a given point on the substrate and a formula was derived for the film thickness distribution.

The geometry of the source-substrate configuration is shown in Figure 3.2. Let N be the rate at which particles are sputtered in different directions from a point source $d\sigma$ on the target erosion ring. Then the number of particles that pass through the solid angle $d\Omega$ in a direction forming an angle α with the normal to the target in unit time is

$$dN = CNf(\alpha)d\Omega\,, \tag{3.3}$$

where $f(\alpha)$ is the angular distribution of sputtered particles and C is the normalization factor to make $\int dN = N$.

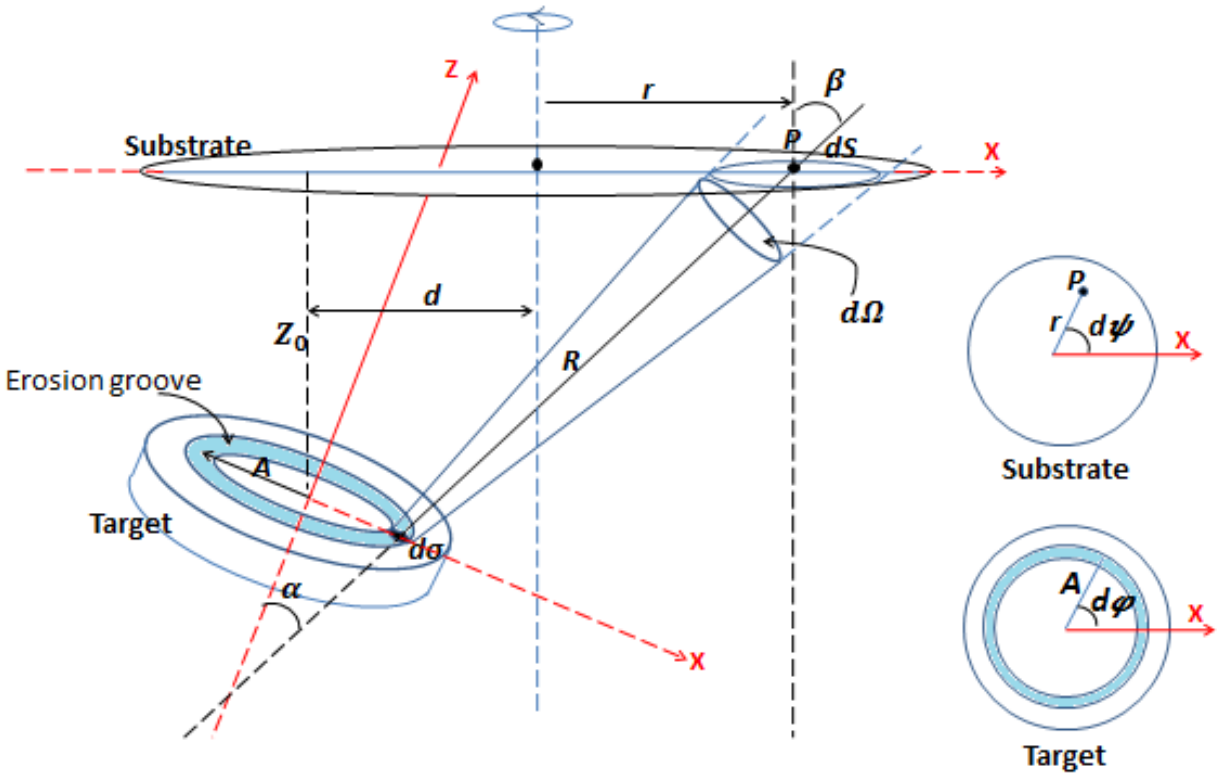

Figure 3.2: The source-substrate configuration

If the particles arrive at area dS on the substrate inclined at an angle β with respect to the direction of emission, the flux of particles at point P is given by

$$\frac{dN}{dS} = \frac{CNf(\alpha)\cos\beta}{R^2}, \tag{3.4}$$

where R is the distance between the point source on the target and point P on the substrate and $d\Omega$ has been substituted with $\frac{dS\cos\beta}{R^2}$.

The receiving flux at point P, due to the whole erosion ring, can be calculated by integrating Equation 3.4 over the erosion ring area:

$$F(P) = \int_0^{2\pi} CN \frac{f(\alpha)\cos\beta}{R^2} \, d\varphi, \tag{3.6}$$

where φ is the azimuthal angle of $d\sigma$.

It should be noted that for a target with a wide area of utilization the approximation of the ring source is not very accurate. In that case, the erosion profile of the target can be measured and defined as a function of the target's radius. This function should then be included in Equation 3.6 and the integration will be performed over the radius as well as the angle. In the original model, the erosion profile was not considered, however, a script has been included in the computer program that calculates the thickness based on the erosion profile. It is important to note that the erosion profile changes as the target is being used so it should be re-measured and entered into the program periodically.

Since the substrate is rotating around its central axis, all the points on the substrate at distance r from the center will receive the same flux. Thus the total flux at a point having the distance r from the substrate's center is given by

$$Flux(r) = \frac{1}{2\pi}\int_0^{2\pi} F(P)\, d\psi = \frac{1}{2\pi} CN \int_0^{2\pi}\int_0^{2\pi} \frac{f(\alpha)\cos\beta}{R^2} \, d\varphi \, d\psi, \tag{3.7}$$

where ψ is the azimuthal angle of dS.

Earlier we assumed that once the sputtered atoms reach the substrate they do not diffuse, reflect or evaporate. Therefore the flux of particles reaching any point on the substrate is proportional to the thickness of the film at that point. Consequently, thickness can be expressed in terms of Equation 3.7 by including a proportionality constant:

$$T(r) = \frac{I}{2\pi} \int_0^{2\pi} \int_0^{2\pi} \frac{f(\alpha)\cos\beta}{R^2} \, d\varphi \, d\psi \, , \tag{3.8}$$

where I includes all the constant quantities and its value will be determined by fitting the experimental results to the simulation.

Equation 3.8 is the basic formula for all further calculations. Based on the coordinate system that is shown in Fig.3.2, all the quantities in Equation 3.8 can be expressed in terms of d, Z_0, A, and r.

Determining the angular distribution of sputtered particles, $f(\alpha)$, is discussed in the following section.

3.1.2 Angular Distribution of Sputtered Atoms

The emitting characteristic of the sputtered particles depends on multiple factors such as the bombarding ions' kinetic energy, the crystal structure of the target, and the ions' angle of incidence [3-4]. In order to quantitatively determine the angular distribution, a detailed understanding of the interactions between the ions and target material is required. For this matter, one has to consider an accurate model for interaction potentials, the energy transfer mechanism in atomic collisions, surface and bulk properties of the target, and finally the penetration phenomena. The quantitative derivation of the angular distribution is beyond the scope of this thesis; however, this section is intended to give an overview of the ion-target interactions for different sputtering regimes and discuss the angular distribution that was used in our model.

Ion-Target Interactions

Physical sputtering is effectively a momentum and energy transfer process. Most of the studies use a classical two-particle elastic scattering model as a starting approximation to describe the sputtering process.

Upon impingement of an ion (e.g. Ar^+) on the target surface, the elastic collision between the nucleus of the energetic ion and the target atoms transfer part of the ion's kinetic energy and momentum to the target atoms. Depending on the ion energy, three different sputtering regimes can be identified for the elastic collisions of ions and target atoms: The single knock-on (low energy), the linear cascade (intermediate energy) and the spike regime (high energy).

In the single knock-on regime the energy transferred from the ion to the target is sufficient to generate a small number of primary recoils. The recoil atoms can escape the surface if they are energetic enough to overcome the surface binding energy and also have a momentum component normal to the surface. In the linear cascade regime the incident ion produces a cascade of atom displacements and the recoil atoms may have sufficient energy to generate the secondary knock-ons. In the linear regime, the density of recoils is sufficiently low to ensure that most collisions involve one moving and one stationary particle. Finally in the spike regime, the spatial density of recoils is so high that the majority of atoms within a certain volume are moving. Each primary recoil in the spike regime can initiate an independent subcascade [3-5].

The single knock-on regime is valid in the low ion energy range (<1 *keV*), unless the ions are very light where, due to an inefficient energy transfer, the energy range can be extended to the lower *keV* region. For *keV* and *MeV* ions, the linear cascade best describes the process except for very heavy ions which are stopped rapidly and generate spikes. Most of sputtering processes are performed in the energy range that falls into the linear cascade regime. Magnetron sputtering, however, is a low energy sputtering technique and the energy of ions is generally in the range of several hundred *eV* which puts magnetron sputtering in the lower energy range of linear cascade and/or single knock-on [3-5].

Surface and Volume Factors

The particle that is sputtered from the target due to the ions bombardment possesses energy and momentum whose values are the result of the interference of volume (cascade) and surface factors. The surface factors include the ion's angle of incidence and target atom's surface binding energy. The volume factors are determined by the interactions between the ions and target atoms that, as discussed, depend on the ion's kinetic energy. The combination of all these factors determines the energy and momentum transferred to the sputtered particles and the same factors influence their angular distribution as well. It should be noted that the angular distribution is also affected by the crystal structure of the target. The correlation was discovered once Wehner observed that the atoms of a single crystal metallic target are preferentially ejected in the directions of closest packing, that is [110] in bcc, [111] in the fcc lattice and diamond structure [3-6]. However, both experiments and simulations show that this crystalline behaviour disappears in low energy sputtering (<0.5 *keV*) [3-7].

Angular Distribution

There have been numerous theoretical calculations and simulations to obtain a formula for the angular distribution of sputtered particles. One of the early theoretical expressions of the angular distribution was provided by Sigmund and Thompson for the linear cascade regime that is of interest in many of the sputtering processes [3-8, 9]. One of the main assumptions of Sigmund-Thompson theory was that of a complete collision cascade that results in a complete isotropic recoil distribution. Based on this assumption, they predicted that the angular distribution of the sputtered particles should follow a cosine distribution. Many analytical models of the sputtering process have been proposed based on the Sigmund-Thompson theory and their predictions for the thickness distribution are in good agreement with the experimental results [3-10]. However, deviations from the cosine distribution have been observed primarily for light ions with low incident energies and heavy ions with high incident energies. For low incident ion energies, the collision cascade is formed but it is not well developed which leads to a non-isotropic recoil distribution.

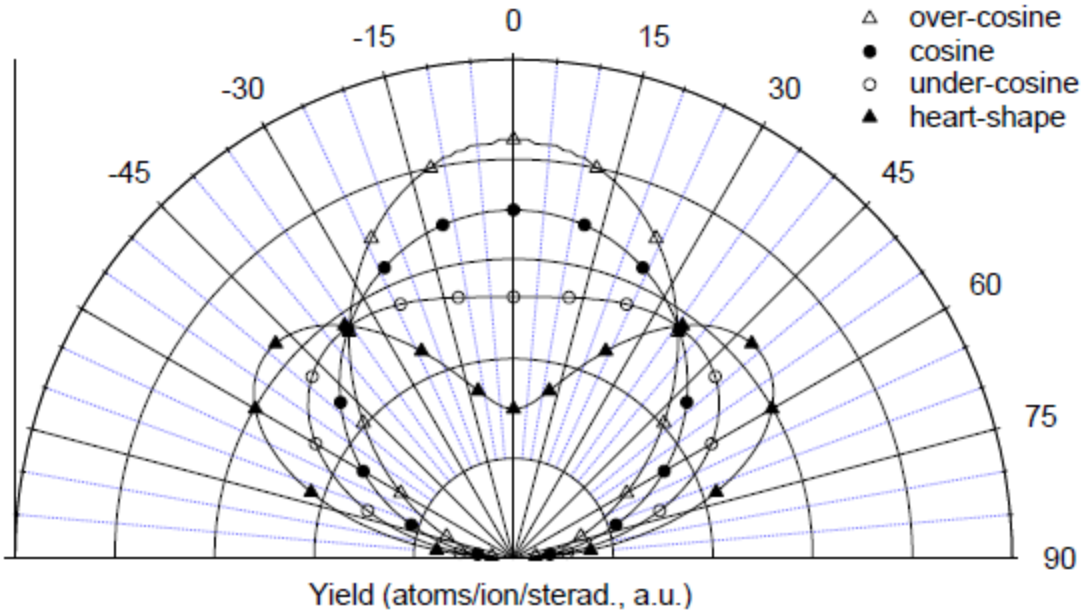

Figure 3.3: Different types of angular distribution

In this case, the angular distribution is under-cosine or heart-shaped (enhanced emission at oblique angles) [3-11]. For high incident energies, the angular distribution tends to be over-cosine (higher emission near the surface normal). Figure 3.3 shows the different types of angular distribution of sputtered particles. In order to better predict the various film thickness profiles, the angular distribution was chosen to be proportional to $(\cos\alpha)^n$ to reproduce the under (n <1) and over cosine (n >1) distributions [3-4]. α is the angle between the normal to the surface of the target and the direction of emission and n is the fitting parameter.

The draw back with the $(\cos\alpha)^n$ distribution is that it cannot produce the heart-shaped distribution which is the case in the magnetron sputtering where the ions energies are very low (<500 *eV*). In a sputtering discharge, the average energy of ions bombarding the target is governed by the discharge voltage that is approximated with the DC bias voltage (V_{DC}) in the case of RF sputtering, as discussed in Chapter 2. In this experiment, V_{DC} ranges from 167 *V* to 188 *V* for different source-substrate distances. Simulations have shown that the average energy of ions is approximately 75% of the discharge voltage [3-12, 14].

Yamamura *et al.* [3-15, 16] proposed an alternative equation for the angular distribution at normal incidence that has the following form:

$$f(\alpha) = \cos(\alpha)[(1 + b\cos^2(\alpha)] \,, \tag{3.9}$$

where b is the fitting parameter. The cosine distribution corresponds to $b = 0$, $b > 0$ gives the over-cosine shape, $-0.5 < b < 0$ generates the under-cosine distribution while $b < -0.5$ corresponds to the heart-shaped profile.

Between the two distribution functions that were discussed, Equation 3.9 was chosen to represent the angular distribution of sputtered particles in our experiments since it best fit the experimental results.

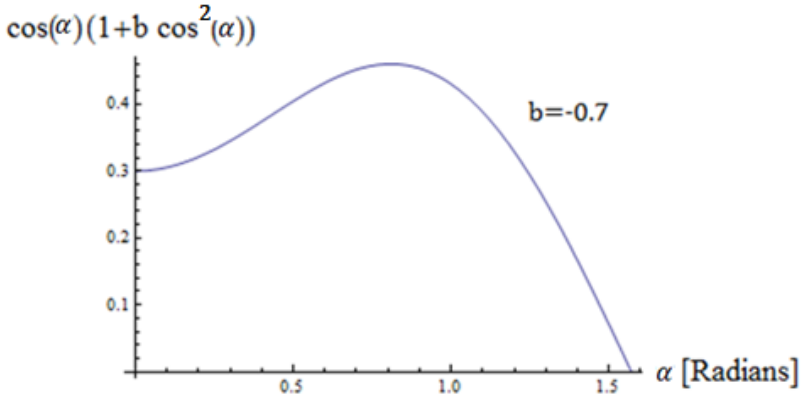

Figure 3.4: Yamamura's angular distribution function

Figure 3.4 shows the Yamamura's distribution function for $b = -0.7$ which is close to the b values obtained in our simulations. As is clear from Equation 3.9, the shape of the distribution function depends on the parameter b.

Yamamura also found an expression for b that in the case of normal incidence reduces to the following form:

$$b = \frac{5}{3}\left(\frac{E_{th}}{E}\right)^{1/2} \Big/ \left[1 - \left(\frac{E_{th}}{E}\right)^{1/2}\right], \tag{3.10}$$

where E is the incident ions' energy and E_{th} is the target threshold energy. The sputtering threshold is defined as the kinetic energy of the incident ions below which no observable sputtering occurs. Since the deposited energy on the target from the incident ions depends on the angle of incidence and collision mechanism, calculating the threshold energy is not very straightforward. Thus the correlation between Equation 3.10 and b as a fitting parameter has not been well established.

The values of b obtained from the simulation are presented in Section 3.3.

3.2 Experimental Procedure

3.2.1 Sample Deposition

Silicon films were deposited from a silicon target onto a rotating glass substrate. Prior to deposition, the glass substrates were cleaned in an ultrasonic cleaner filled with methanol. Substrates were then rinsed with de-ionized water and blow dried by nitrogen gas. Prior to the deposition the vacuum chamber was pumped down to a base pressure of 1×10^{-7} *torr*. The deposition process was carried out in the argon atmosphere using a 3-inch MeiVac magnetron source in a high vacuum, the Radio Frequency (13.56 *MHz*) sputtering system manufactured by Kurt. J. Lesker. The target was an N-type single crystal of (<110>) silicon with resistivity of 0.1-0.5 *ohm.cm*, a diameter of 3 inches and a thickness of 2.5 inches. The diameters of the glass substrates were 6 inches. During the deposition, the process power, pressure and time were set at 100 *W*, 0.75 *mtorr*, and 15 minutes respectively.

Figure 3.5 shows the different source-substrate configurations. Two sets of samples were deposited for this study and in total seven samples were prepared. For the first set of samples, the silicon target was clamped onto a sputtering gun that was inserted into the chamber at "Gun position 1" as it is shown in Fig.3.5. The sputtering gun makes an inclination angle of $17°$ with respect to the normal line to the substrate and it is free to move along this direction so it was set at 3 different positions that are labelled as 1, 2 and 3 in Fig.3.5. For each of these positions, we can consider a vertical distance (Z_0) and horizontal offset (d) between the centers of the target and the substrate (Fig.3.1)

For the second set of samples, the sputtering gun was inserted into the chamber at "Gun position 2" making the same inclination angle of 17°. This time, the gun was set at 4 different positions with different Z_0 and d values. These positions are labelled as 4, 5, 6, and 7 in Fig.3.5. The horizontal offset (d) values for the second set of samples are relatively smaller than the offsets for the first set.

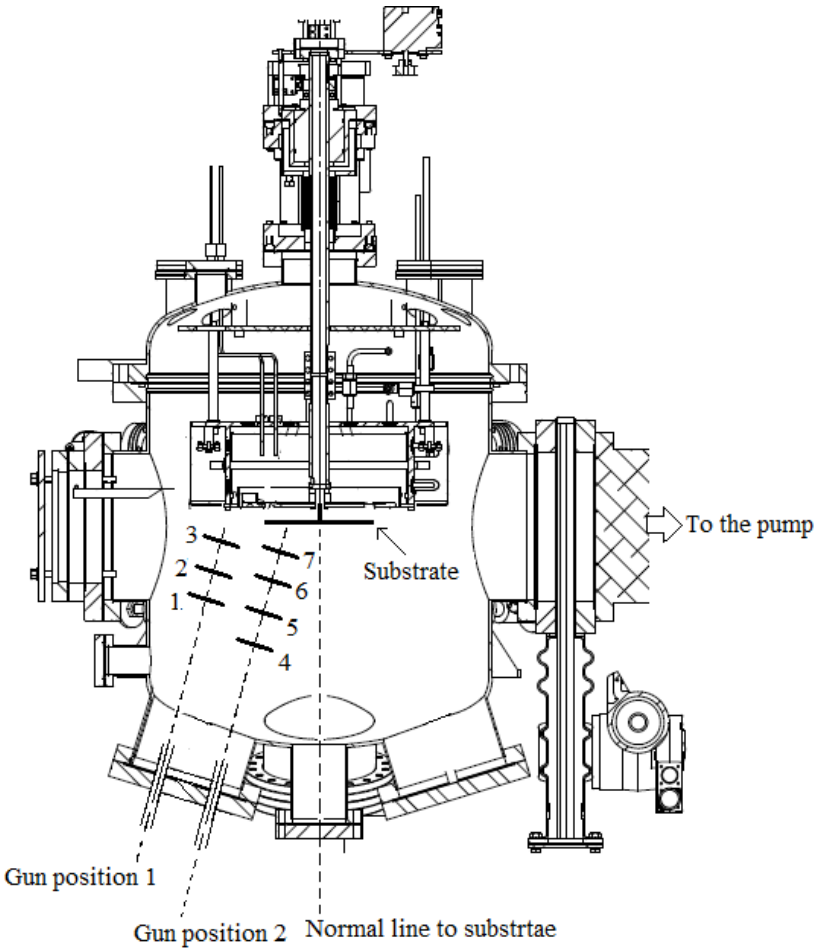

Figure 3.5: Different source-substrate configurations. The dashed lines show the direction of the sputter guns that are not shown in the figure.

Since the inclination angle of the sputter gun was kept constant at 17°, Z_0 and d values for each of the positions are correlated.

Initially, all the samples were deposited at room temperature; however, due to the roughness of the films I was not able to perform thickness measurements by means of the X-ray reflectivity method. In the X-ray reflectivity measurement, the angle of

incidence is shallow and somewhat parallel to the film's surface. If the surface is not ideally smooth, the X-rays can be scattered in any direction. In order to reduce the roughness of the films for our samples, the deposition temperature was raised to 400℃. The deposition time, power, pressure and temperature were maintained constant for all the experiments to ensure consistency.

3.2.2 Thickness Measurements

The thickness of the deposited films was determined by the grazing incidence X-ray reflectometry (GIXR) measurement. GIXR is a surface-sensitive technique to characterize surfaces and interfaces of thin films and multilayers. The thickness of a film can be calculated from the interference fringes produced by the reflected X-rays in the specular direction. The thickness measurements were performed in a Panalytical X'Pert PRO MRD with polarized collimated Cu K_α X-rays with a wavelength of 1.5418 $\AA$.

When a wave crosses the interface between the vacuum and matter, its wave vector changes from K to nK where n is the index of refraction. The complex index of refraction in the X-ray region is smaller than 1 and is given by:

$$\mathrm{n} = 1 - \delta - \mathrm{i}\beta\,, \tag{3.11}$$

where δ and β represent the dispersion and absorption, respectively. These parameters are related to the atomic scattering factors [3-17].

For all the elements, δ is a positive quantity in the energy region away from the absorption edges so the real part of the refractive index is smaller than unity, and therefore the total reflection of X-rays can be observed if the incident angle is greater than the critical angle. The critical angle of total reflection, θ_c, is usually on the order of 0.1° to 1°.

When the X-ray enters the material with incident angles smaller than θ_c, at every interface, a portion of the X-ray is reflected and the rest is refracted. Interference of the

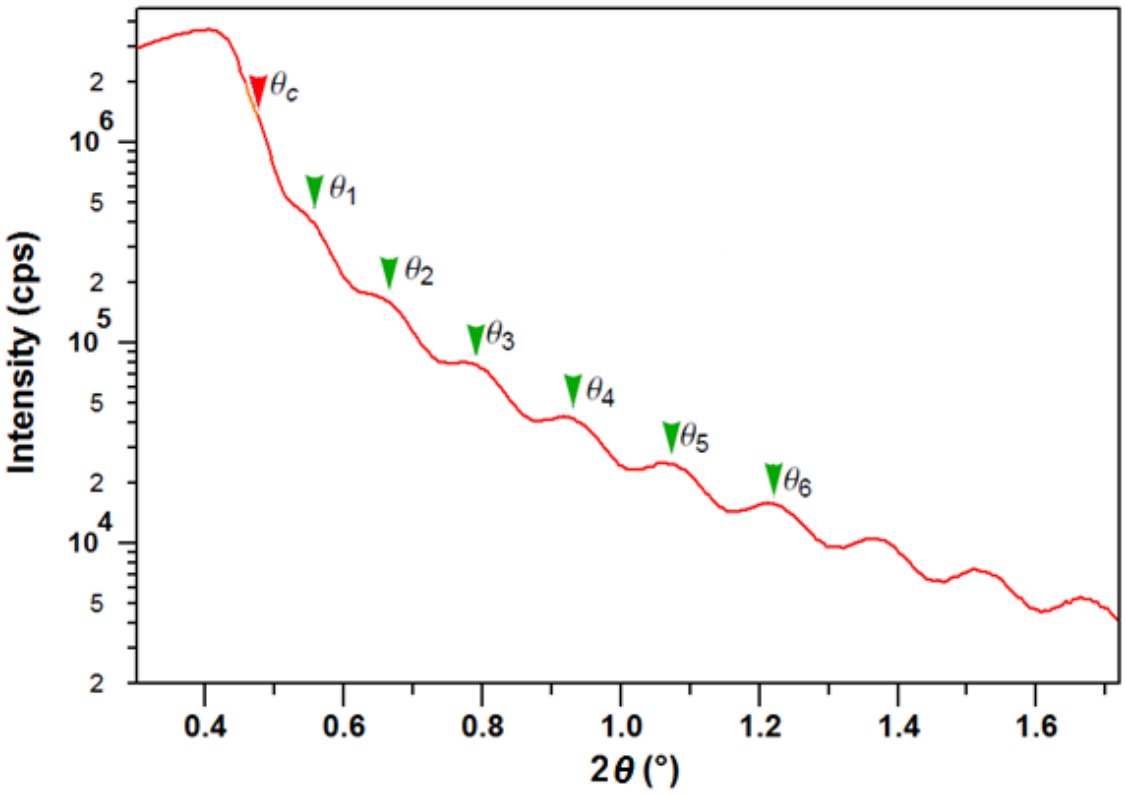

Figure 3.6: The X-ray reflectivity curve from a silicon film. The peaks, θ_1, θ_2, ….. are due to constructive interference between X-rays reflected from the surface and those reflected from the interface with the substrate. θ_c is the critical angle.

partially reflected X-ray beams from the interfaces creates an interference pattern known as Kiessig fringes (shown in Figure 3.6). In the case of one component film, the X-rays reflect from the top surface and substrate interface. The thickness of the layer is determined by the period of fringes.

Figure 3.7 shows a ray diagram of the optical paths between reflected X-ray beams in a $\theta - 2\theta$ scan. In order for constructive interference to occur, the optical path length difference between the two beams must be an integer multiple of the wavelength.

Assuming that the index of refraction of the film is n_1,the difference in the optical path (ΔL) between the reflected beams is given by:

$$\Delta L = n_1(AB + BC) - AD \, . \tag{3.12}$$

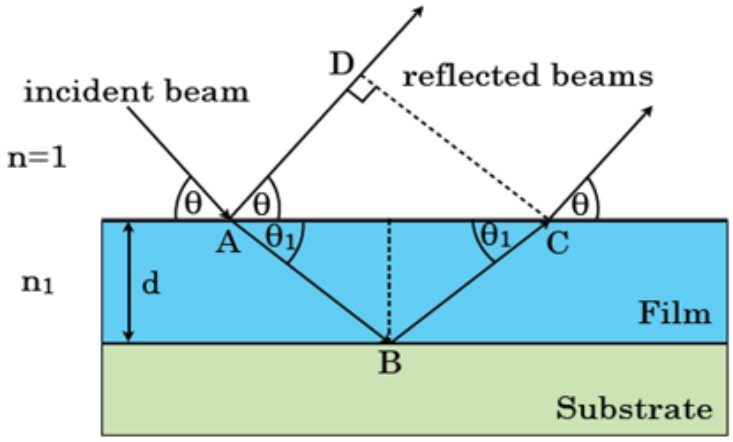

Figure 3.7: The optical paths of X-rays reflected from the top and bottom surface in a single component film with thickness of d and refraction index of n_1. θ and θ_1 are the complemetary angles of incidence and refraction respectively.

As shown in Fig.3.7, the optical path lengths AB and BC are identical and equal to:

$$AB = BC = \frac{d}{\sin\theta_1}. \tag{3.13}$$

The optical path length AD can also be written in terms of d:

$$AD = AC\cos\theta = 2AB\cos\theta_1\cos\theta = 2\frac{d}{\sin\theta_1}\cos\theta_1\ \cos\theta. \tag{3.14}$$

The refracted angle, θ_1, is determined from Snell's law:

$$\cos\theta_1 = \frac{n\cos\theta}{n_1} = \frac{\cos\theta}{n_1}, \tag{3.15}$$

and n_1 can be written in terms of the critical angle, θ_c:

$$n_1 = \cos\theta_c. \tag{3.16}$$

The condition required to have constructive interference is $\Delta L = m\lambda$, where m is an integer and λ is the wavelength. Equation 3.12 can now be written in terms of Equations 3.13, 3.14 and 3.16 with the interference peaks labeled by an incident angle, θ_m:

$$\Delta L = 2\cos\theta_c \frac{d}{\sin\theta_1} - 2\frac{d}{\sin\theta_1}\cos\theta_1\cos\theta_m = m\lambda\,. \tag{3.17}$$

By using trigonometric identities and replacing θ_1 with θ_m from Equation 3.15, the simplified equation for the constructive interference is:

$$m\lambda = 2d\sqrt{\cos^2(\theta_c) - \cos^2(\theta_m)}\,, \tag{3.18}$$

that can be written in the more well-known form of:

$$m\lambda = 2d\sqrt{\sin^2(\theta_m) - \sin^2(\theta_c)}\,. \tag{3.19}$$

The thickness of the film, d, can be calculated from Equation 3.19 based on the peak positions of the Kiessig fringes (θ_m).

The critical angle value, θ_c, is estimated from the interference pattern in Fig.3.6, by determining the angle at which the intensity is half of the maximum value. The silicon film critical angle was determined to be 0.2352°. The thickness of the films was calculated from the slope of $\frac{m\lambda}{2}$ versus $\sqrt{\sin^2(\theta_m) - \sin^2(\theta_c)}$.

3.3 Results and Discussion

The simulated and measured film thickness values for different source-substrate positions are shown in Figures 3.8 and 3.9. The fitting parameters, I and b, are calculated and shown in each figure. The angular distribution function of sputtered particles, $f(\alpha)$, is also shown together with the corresponding thickness distribution profile for each sample. As was discussed earlier, the shape of $f(\alpha)$ is determined by the parameter b.

Figure 3.8 shows the film thickness profiles and angular distribution functions for the first set of samples where the sputtering gun was placed at “Gun position1” as it was shown in Fig.3.5. For these samples the horizontal offsets (d) are relatively large so we expect a thicker film at the edge of the substrates. Figure 3.8 (a), which is for the case with largest

Z_0 value, demonstrates the best uniformity among the first set of samples with the film thickness deviation of $\pm$5% and sputtering rate of 21 *Å/min*.

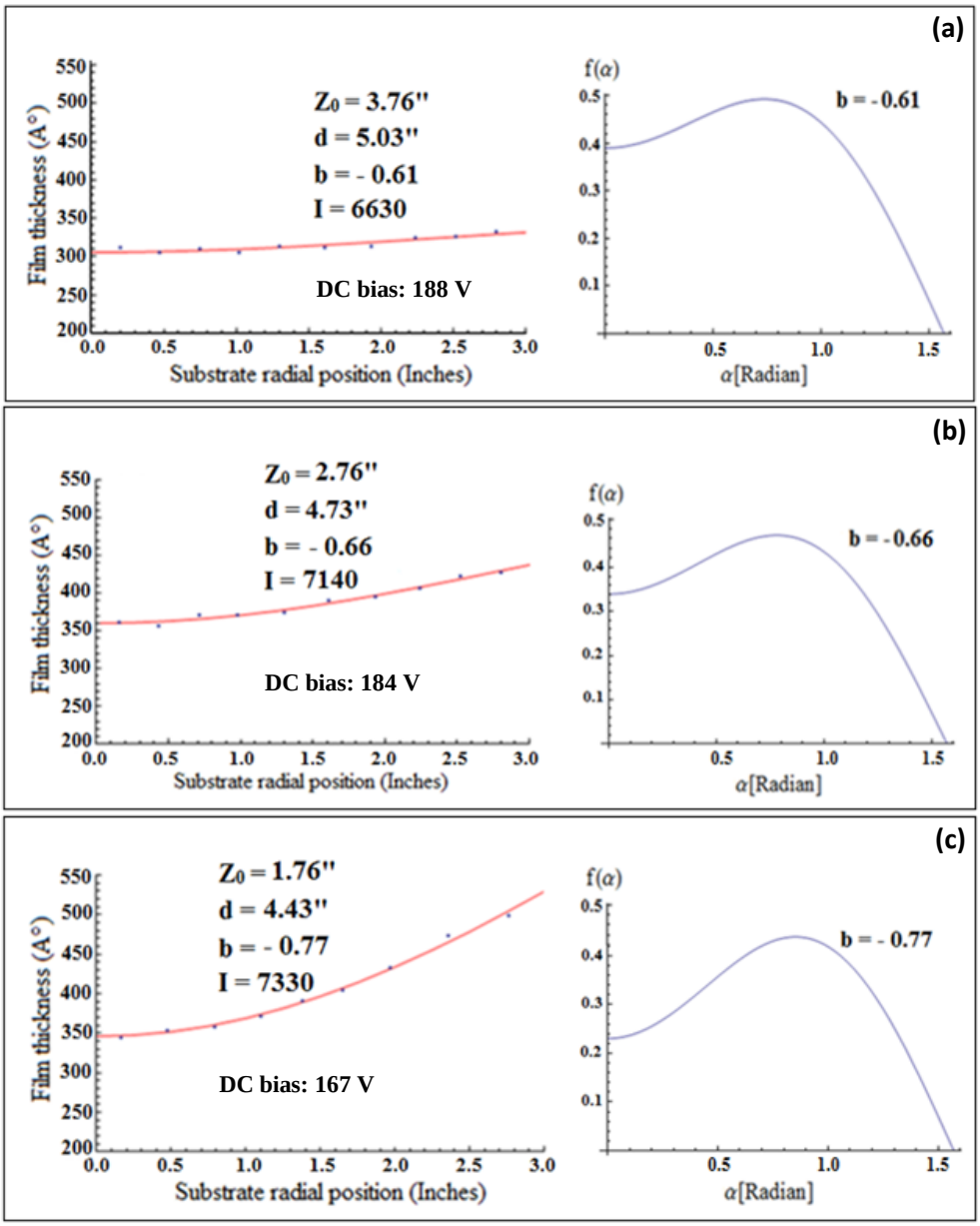

Figure 3.8: Simulated (red lines) and measured (dots) film thickness profiles for the first set of samples at different source-substrate positions. The angular distribution functions are also shown for the corresponding *b* values.

Figure 3.9 shows the film thickness profiles and angular distributions for the second set of samples where the sputtering gun was placed at “Gun position2” as was shown in Fig.3.5

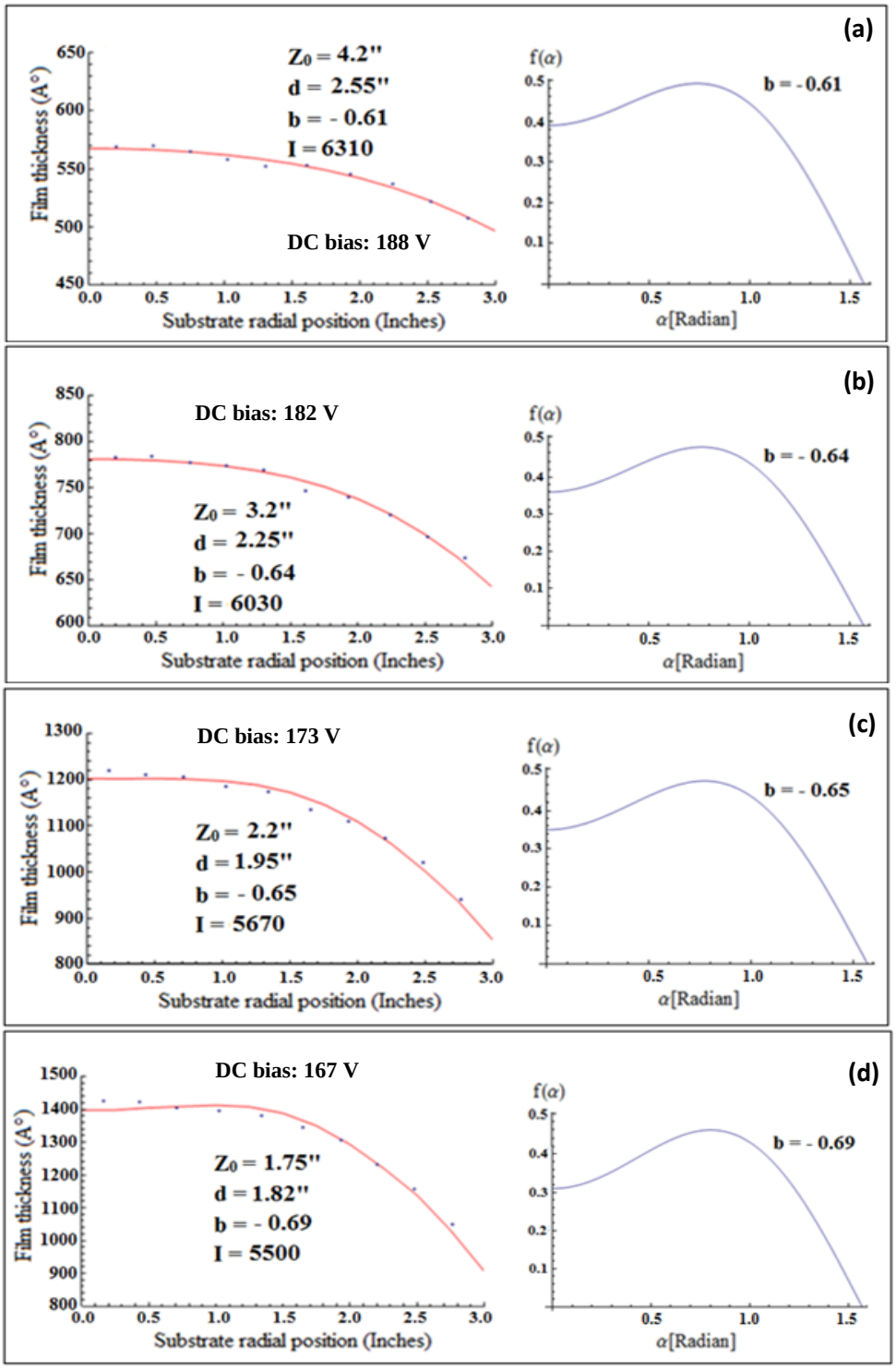

Figure 3.9: Simulated (red lines) and measured (dots) thickness profiles for the second set of samples at different source-substrate positions. The angular distribution functions are also shown for the corresponding *b* values.

For these samples, the horizontal offset (d) is relatively small which leads to a thicker film in the center of the substrates. The best uniformity for the second set of samples belongs to the film in Fig.3.9 (a) (largest Z_0) with the film thickness deviation of $\pm$7% and the sputtering rate of 34 *Å/min*. For these samples, the quality of the fit diminishes as Z_0 and d are decreased and it could be related to the fact that silicon is sputtered from the substrate as well as the target.

The sputtering rates for two sets of samples were achieved using 100W RF input power. Further increase in the sputtering rate can be obtained by increasing the RF power. The maximum power generated by our RF power supply is 600W.

As it is shown in Fig.3.8 and Fig.3.9, both I and b values change as the relative source-substrate positions change. The potential dependence of I and b on the geometry of the system is discussed below.

Dependence of I on Geometry

In Equation 3.8 parameter I was chosen to represent the multiplication of three quantities that were considered constant: a normalization factor, a proportionality constant (between flux and thickness), and the sputtering rate (N). It is reasonable to think that the only quantity that may change due to the change in the geometry is the sputtering rate N and that leads to obtaining different values for I. The sputtering rate depends on the energy transferred from the bombarding ions which itself is a function of the ions' energy and angle of incidence. We previously assumed that ions strike the target perpendicularly, so we only need to examine whether the change in the geometry affects the ions' energy or not.

As the distance between source and substrate varies, the discharge voltage V_{DC} fluctuates. The discharge voltage is an indication of the ions' energy; so if V_{DC} changes as the geometry changes, then the ions' energy and sputtering rate will be affected. So the change in the source-substrate distance can in fact have an impact on the sputtering rate and I. However, the correlation between V_{DC} and I as shown in Fig.3.8 is inverse to that of in Fig.3.9. Further study is required to explain this inconsistency.

Dependence of b on Geometry

The values calculated for b from the simulation fall in the range of $0.61 \leq |b_{fit}| \leq 0.77$. As indicated in Fig.3.9 and Fig.3.8, when Z_0 and d are varied, V_{DC} and the absolute value of b changes.

In order to relate the fluctuations in b to the change in the source-substrate geometry, we can take a look to Equation 3.10 that was proposed by Yamamura to predict the value of b in the angular distribution formula (Equation3.9).

$$b_{theory} = \frac{5}{3}\left(\frac{E_{th}}{E}\right)^{1/2} \Big/ \left[1 - \left(\frac{E_{th}}{E}\right)^{1/2}\right]. \qquad (3.10)$$

According to Equation 3.10, b_{theory} is inversely proportional to the energy of the bombarding ions (E) and subsequently to V_{DC}. This correlation is consistent with the simulation results that suggest the absolute value of the b parameter decreases as V_{DC} increases and vice versa.

Equation 3.10 also suggests that b_{theory} depends on the target threshold energy (E_{th}). However, finding the correlation between E_{th} and the geometry is more complicated as the ion-target collision mechanism should be known. So it is not clear to what extent E_{th} and E may contribute to the deviations in b values as the source to substrate distance changes. Also, to numerically calculate b_{theory}, the values of E and E_{th} should be determined precisely since the value of the b parameter is sensitive to these quantities. Further study is required to determine the values of E and E_{th}. In order to determine the effect of geometry on E and E_{th}, I suggest depositing more samples from different materials under different sputtering conditions.

In the end, from the good agreement between the simulated and measured film thickness distributions it can be concluded that the choice of angular distribution function and other simplifying assumptions were valid for the experimental conditions employed.

3.4 Conclusion

In this study, a theoretical model was derived to predict the thickness distribution of silicon films deposited from an off-axis, inclined, circular magnetron source onto rotating substrates. The aim of this work is to investigate the effect of source-substrate geometry on the thickness distribution and for this reason several assumptions were made to simplify the model so it solely depends on the geometrical quantities. Based on the sputtering regime in our experiments, Yamamura's function was employed to demonstrate the angular distribution of sputtered particles for normal incident ions. A computer program including two fitting parameters was developed using Mathematica to numerically calculate the thickness profiles.

In order to verify the model, a total of seven samples were deposited at different source-substrate positions while all other experimental conditions including power, pressure, time, and temperature were maintained constant. The thickness of the deposited films was then measured using the X-ray grazing incidence angle method. Finally, the experimental data were fitted to the simulated profiles and a good correlation between the simulation and experiment was demonstrated. According to the calculated fitting parameters, the angular distribution of sputtered particles in our experiment follows a heart-shaped distribution for all the samples. Further studies need to be carried out to establish a solid relation between the fitting parameters and the experimental conditions.

It is expected that the simulation program will help predict the optimum geometry for a specific target material with a known erosion profile.

For future work, I suggest investigating the effects of the inclination angle of the sputtering source, pressure, power, target material, and erosion profile on the thickness distribution. The effect of the erosion profile on thickness distribution is specifically important since it has to be considered when designing the magnetic field profile for the sputtering source since the best target utilization does not necessarily give the best film thickness uniformity [3-22].

Refereces

[3-1] X. S. Du, Y. D. Jiang, J. S. Yu, J. Li, and G. Z. Xie, *Quantitative evaluation of film thickness uniformity: Application to off-axis magnetron source onto a rotating substrate*, Journal of Vacuum Science & Technology A 25, 215 (2007).

[3-2] S. Swann, S. A. Collett, and I. R. Scarlett, *Film thickness distribution control with offaxis circular magnetron sources onto rotating substrate holders: Comparison of computer simulation with practical results*, Journal of Vacuum Science & Technology A 8, 1299 (1990).

[3-3] Wolfram Research, Inc., Mathematica, Version 9.0, Champaign, IL (2012).

[3-4] Zhu Lin Zhang & Lai Zhang*, Anisotropic angular distribution of sputtered atoms, Radiation Effects and Defects in Solids: Incorporating Plasma Science and Plasma Technology*, May 2004, Vol. 159, pp. 301–307.

[3-5] J. M. Walls, *Methods of Surface Analysis: Techniques and Applications*, Cambridge University Press (1989).

[3-6] G.K. Wehner, J. Appl. Phys. 26 (1955).

[3-7] Rainer Behrisch, Wolfgang Eckstein, *Sputtering by Particle Bombardment: Experiments and Computer Calculations from Threshold to MeV Energies*, Springer (2007).

[3-8] M. W. Thompson, Philos. Mag. 18 (1968).

[3-9] P. Sigmund, *Theory of Sputtering. I. Sputtering Yield of Amorphous and Polycrystalline Targets*, Phys. Rev. 184 (2), 383 (1969).

[3-10] Diederik Depla and Stijn Mahieu, *Reactive sputter deposition*, Springer Science & Business Medi, June 2008.

[3-11] H. H. Andersen, *Beam Interactions with Materials and Atoms,* Nuclear Instruments & Methods in Physics Research Section B, 33(1-4), 466–473 (1988).

[3-12] S. Mahieu and D. Depla, Journal of Physics D-Applied Physics 42 (5), 053002 (2009).

[3-13] D. Czekaj, B. Goranchev, E. K. Hollmann, V. A. Volpyas, and A. G. Zaytsev, Vacuum 42 (1-2), 43 (1991).

[3-14] M. J. Goeckner, J. A. Goree, and T. E. Sheridan, IEEE Transactions on Plasma Science 19 (2), 301 (1991).

[3-15] Y. Yamamura, Radiation Effects and Defects in Solids 55 (1-2), 49 (1981).

[3-16] Y. Yamamura, T. Takiguchi, and M. Ishida, Radiation Effects and Defects in Solids 118 (3), 237 (1991).

[3-17] Albert C. Thompson, Douglas Vaughan, *X-ray Data Booklet*, Lawrence Berkeley National Laboratory, Second edition, January 2001.

[3-18] G. K. Wehner, Phys. Rev. 102, 690 (1956).

[3-19] W. Eckstein, C. Garcia-Rosales, J. Roth, and J. L´aszl´o. *Threshold Energy for Sputtering and its Dependence on Angle of Incidence*. Nuclear Instruments and Methods in Physics Research B, 83(1-2):95–109 (1993).

[3-20] Y. Yamamura and H. Tawara. *Energy Dependence of Ion-Induced Sputtering Yields from Monatomic Solids at Normal Incidence*, Atomic Data and Nuclear Tables, 62(2):149–253 (1996).

[3-21] V. G. Sevast'yanov, P. Ya. Nosatenko, V. V. Gorskii, Yu. S. Ezhov, D. V. Sevast'yanov, E. P. Simonenko, and N. T. Kuznetsov, *Experimental and Theoretical Determination of the Saturation Vapor Pressure of Silicon in a Wide Range of Temperatures*, Russian Journal of Inorganic Chemistry, Vol. 55, No. 13, pp. 2073–2088 (2010).

[3-22] S. Swann, *Film Thickness Distribution in Magnetron Sputtering*, Vacuum 38 (8-10), 791-794 (1988).

Chapter 4

Enhancing the Crystallization and Texture of Silicon Films Using a Copper Seed Layer

Introduction

During the past few decades, polycrystalline silicon (PCS) thin films have become popular due to their wide range of applications in the semiconductor industry, from thin film transistors for microelectronic applications and electronic display devices to solar cells.

The conventional way to obtain polycrystalline silicon is by low pressure chemical vapour deposition method at high temperatures (≥550℃) [4-1]. PCS thin films are also fabricated by crystallizing amorphous silicon (a-Si) thin films. The a-Si film is usually crystallized by techniques that require annealing treatments such as solid phase crystallization (SPC) (≥700℃) [4-2, 3], solid phase epitaxy on crystalline silicon (≥450℃) [4-4], excimer laser annealing [4-5], and metal induced crystallization (MIC) [4-6]. However, among all these techniques, MIC is promising since it is a relatively low cost crystallization method compared with laser annealing and also, it needs a lower processing temperature and shorter annealing time compared with SPC. Therefore, cheaper substrates such as glass can be substituted for the expensive silicon wafers, quartz or Pyrex in the fabrication process.

There have been many studies on MIC of Si using various metals. In one of the studies [4-7], W. Knaepen *et al.* investigated the effect of 20 different metals on the crystallization temperature of Si and the results are shown in Figure 4.1. Crystallization temperatures shown in Fig.4.1 are only valid for the specific experimental conditions in the related study.

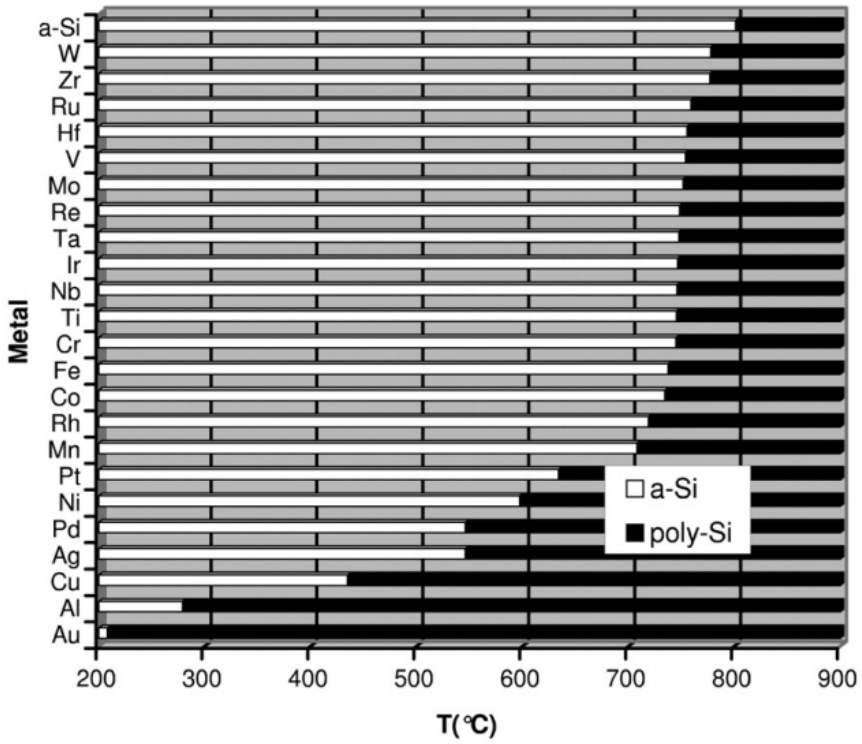

Figure 4.1: The summary of the influence of a metal film on the crystallization temperature of a-Si. All samples are composed of 30 *nm* metal deposited on top of 200 *nm* Si and annealed at the rate of 3℃/s.

Fig.4.1 clearly shows the influence of metal films on the crystallization temperature of silicon. According to W. Knaepen *et al.*, the sample without a metal film had a crystallization temperature of 780℃ and all the metal films used in the study lowered this temperature.

As part of my Master's thesis, I studied the physics of MIC in the silicon-copper system. Cu-induced crystallization of Si has several applications in microelectronics [4-8] and recording industry [4-9].

In this thesis, the crystal structure of sputter-deposited silicon on a thin layer of copper was investigated by using X-ray diffraction (XRD) measurements. The formation of a silicide phase was observed after annealing the samples (300−500℃) and the effect of Cu on reducing the crystallization temperature of Si was examined and the results are presented in Section 4.3.

4.1 Metal Induced Crystallization (MIC)

Amorphous silicon has a higher free energy than poly-Si or crystalline silicon. This is the driving force behind the crystallization of a-Si. Upon annealing the a-Si film without any pre-existing crystalline interface or crystalline seed layer, the phase transition from a-Si to poly-Si starts with random nucleation of crystalline clusters in the a-Si matrix [4-10]. The nuclei then grow into crystals by further annealing.

For silicon the activation energy of nucleation is larger than that of crystallization. So if low temperature annealing is used for crystal growth, nucleation can be kept at a minimum level while crystal growth continues from the existing nuclei and large crystal grains can be obtained. Besides obtaining large crystal grains, it is important to start nucleation at a controlled location.

Metal induced crystallization was investigated as a relatively low cost method in an attempt to reduce the crystallization temperature of a-Si and obtain a large grain size. It also allows for control of the nucleation sites. In MIC, the a-Si film is deposited in contact with a layer of suitable metal. The metal-silicon bilayer is then annealed at temperatures ranging from 150℃ to 700℃ for the duration between couple of minutes to several hours leading to the crystallization of the silicon. The main problem with MIC is metal contamination in the crystallized silicon.

In a variant of MIC, metal induced lateral crystallization (MILC) and field-aided lateral crystallization (FALC) have been introduced as attempts to lower contamination by metal catalysts.

In MILC, metal is only deposited on some areas of the a-Si film. Upon annealing, crystallization starts from the portion of the a-Si that is in contact with metal and grows

laterally toward regions that are not covered by metal. In other words, the flux of the diffusing species (metal) is governed by the concentration gradient. The lateral crystallization mechanism is different for different metals and it also depends on the pattern of metal deposited on top of a-Si film [4-11]. MILC is favourable in processes where metal contamination should be minimized in the silicon film. For example in the case of thin film transistors, metal is deposited in the drain/source area and the channel is laterally crystallized [4-12].

In the FALC process, the flux of the diffusing species is controlled by both the concentration gradient and the applied electric field. The application of a DC electric field increases the crystallization rate as compared with MIC and MILC [4-13, 14].

Based on the reaction of metal with Si, there are two different mechanisms for the MIC of silicon: a) forming a compound metal silicide and b) eutectic alloy formation. The well-known driving force behind both mechanisms is the reduction of free energy associated with the transformation of a-Si into polycrystalline Si [4-15].

Metals such as Ni and Pd, form silicide precipitates in the a-Si matrix after annealing. The silicide precipitates act as nucleation sites for crystallization [4-16]. Experiments show that the density of the metal layer on a-Si film is important since a critical number of metal atoms are required to form the nucleus of the silicide precipitates that can act as the seed for crystallization [4-17].

For compound forming metals, the crystallization at the Si/metal interface does not occur until after the formation of the first stable, most Si-rich silicide phase. Thus the temperature at which silicide forms is the minimum temperature that the crystallization process begins.

On the other hand, metals such as Al, Au and Ag do not form compound silicide forms but a simple eutectic system. One mechanism for the MIC of Si using eutectic metals has been proposed by Nast and Wenham [4-15]. The phenomenon is known as the *layer exchange mechanism* as it relies on the layer exchange of adjacent Si and metal films during the crystallization process. It was suggested that when Si is in contact with certain metals, the electronic screening weakens the covalent bonds in Si. As a result

the conversion of a-Si to poly-Si is more favorable as poly-Si has lower free energy. So the use of metals facilitates the inter diffusion of metal and silicon atoms and annealing activates the nucleation process. Heterogeneous nuclei then start to form that can then be grown into crystals at a low temperature without the need to further increase the number of nucleation sites. Note that both nucleation and crystal growth are thermally activated processes, however, the activation energy needed for crystal growth is lower than that of the nucleation. So once nucleation is activated, there is no need to increase the temperature; the crystal growth will proceed. Keeping the nucleation rate low and under control helps increase the grain size.

W. Knaepen *et al*. experimentally determined the crystallization activation energy for 7 materials that are widely used for the MIC of silicon and the results are presented in Table 4.1 [4-7]. It is evident that the activation energy for the crystallization process is lowered by the presence of all metals.

Metal	E_a (*eV*)	Silicide	Dominant diffusion element
a-Si	4.2	/	Si
Ni	3.5	$NiSi_2$	Ni
Pd	2.8	PdSi	Pd/Si
Pt	1.9	PtSi	Pt/Si
Cu	2.2	Cu_3Si	Cu
Ag	1.8		
Au	1.7		
Al	1.4		

Table 4.1: The crystallization activation energy of a-Si/metal bilayers under thermal annealing.

It is important to note that there are different factors that affect the crystallization temperature for a specific Si-metal bilayer such as the heating rate, annealing method (laser vs. thermal), metal to Si thickness ratio and the deposition method. These factors also influence the grain size, crystallization time and homogeneity of the poly-Si films [4-18].

4.2 Experimental Procedure

4.2.1 Sample Deposition

The samples that I studied for this thesis were deposited at room temperature onto glass substrates using DC and RF sputtering techniques. Prior to deposition, the glass substrates were cleaned in a methanol bath and rinsed in de-ionized water. Ultrasonic agitation was used to aid the cleaning process. Upon removal from de-ionized water the substrates were blow dried using nitrogen gas. All the glass substrates were then deposited with a very thin layer of Tantalum (3 *nm*) using RF sputtering. The Ta layer was used as a means to increase the adhesion between the substrate and other layers. This thin layer of Ta showed an amorphous structure in the TEM and XRD measurements.

To investigate the effect of Cu on the MIC of Si, two types of samples were made. In the first case, a 10 *nm* Cu layer was deposited on the Ta-covered glass substrates followed by 50 *nm* a-Si film forming the final structure of Ta[3 *nm*]/Cu[10 *nm*]/Si[50 *nm*] on glass substrates. Both Cu and Si films were deposited by means of DC sputtering technique. After completing the deposition process the samples were annealed in order to perform MIC. The annealing process was carried out in vacuum inside the sputtering chamber at temperatures: 340℃, 410℃ and 480℃ for 20 minutes.

The second growth process involved the deposition of 50 *nm* Si film on the Ta- covered glass substrates forming a Ta[3 *nm*]/Si[50 *nm*] stack as the reference sample. The reference sample was annealed in the vacuum to 480℃ (that is the maximum temperature used to anneal the previous samples). The copper layer is absent in the second structure so we can compare the microstructural changes in the silicon caused

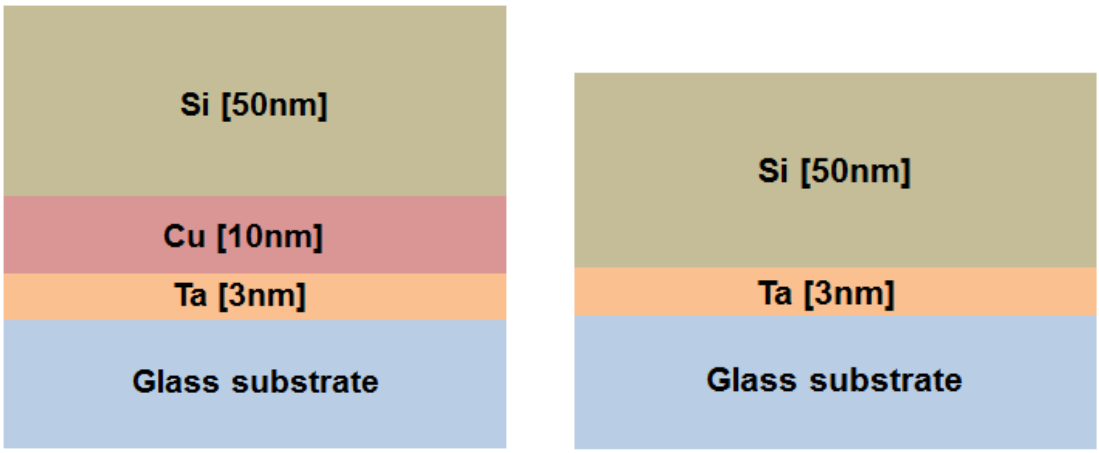

Figure 4.2: The structure of the samples prepared for the experiment. The structure on the right is the reference sample.

by the addition of the Cu layer. Figure 4.2 shows the structure for both types of samples.

As previously stated, the tantalum layer has an amorphous structure and was initially used to increase the adhesion. While this thin layer of Ta did not have any impact on the growth of silicon film in the second structure (Ta[3 *nm*]/Si[50 *nm*]), it enhances the growth of the Cu layer in the [111] direction in the first structure (Ta[3nm]/Cu[10nm]/Si[50nm]).

All depositions were carried out after the base pressure of the chamber had reached at least 1×10^{-7} *torr* so the consistency in the quality of the films is assured. The Cu layer was deposited in a 2.2 *mtorr* argon atmosphere at 134 *W* using a 2-inch Cu target. The Si layer was deposited in a 2.5 *mtorr* argon atmosphere at 150 *W* using a 4-inch silicon target. Unlike Cu that grows along the [111] direction and has an as-deposited fcc structure, the silicon layer is amorphous when deposited.

The microstructural changes of a-Si were then examined by XRD measurements to identify the crystal structure and texture of silicon and other phases formed during the annealing process. The results are presented in Section 4.3.

4.2.2 Structural Characterization

X-ray Diffraction measurement was used as a means to characterize the structure of the films. The XRD measurements were conducted in a Panalytical X'Pert PRO MRD with polarized collimated Cu K_α X-rays with a wavelength of 1.5418 $\AA$.

A symmetric $\theta - 2\theta$ scan was performed to determine the peaks of constructive interference from atomic planes parallel to the surface of the sample. In a symmetric $\theta - 2\theta$ scan the angle between the incident beam and the sample's surface is θ and the angle between the incident beam and detector is fixed at 2θ so that constructive interference is observed solely from reflections off atomic planes and interfaces parallel to the surface of the film. In other words**,** as it is shown in Figure 4.3, $\theta_1 = \theta_2 = \theta$.

The degree of texture within the Si layer was determined by performing an omega scan. In an omega scan the detector is locked at a specific Bragg angle and the sample is tilted so that the plane formed by the incident and reflected beams is perpendicular to the sample's surface in our case. In omega scan θ_3 is fixed while θ_1 and θ_2 are varied; see Fig.4.3.

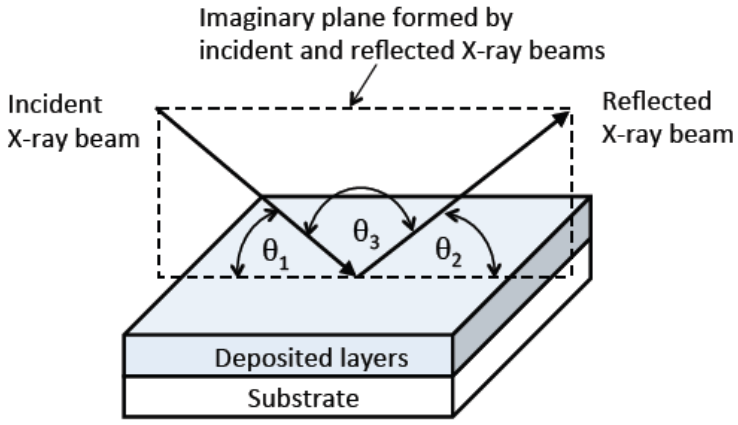

Figure 4.3: The X-ray Diffraction set up. θ_1 is the angle between the incident beam and the surface, θ_2 is the angle between the reflected beam and the surface and θ_3 is the angle between the incident and reflected beams. For all the measurements the plane formed by the incident and reflected beam was perpendicular to the surface.

The full width at half maximum (FWHM) of the omega scan is a measure of the orientation distribution of the layer's planes with respect to the sample's surface. The FWHM was measured for the silicon (111) peak.

4.3 Results

Fig.4.4 shows the XRD spectrum for the reference sample (Ta[3 *nm*]/Si[50 *nm*]) that was annealed to 480℃.

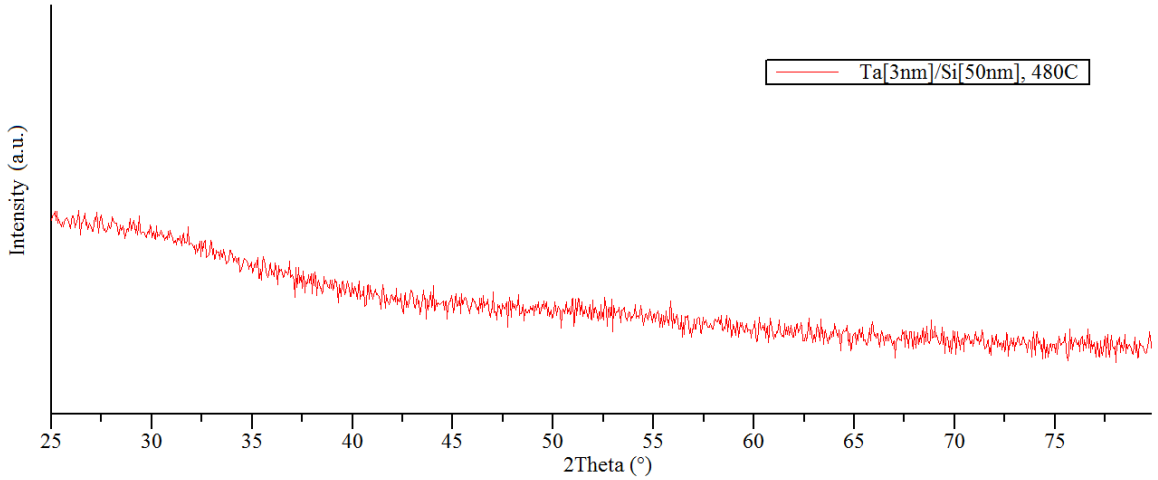

Figure 4.4: The XRD pattern of Ta/Si stack annealed to 480℃

As mentioned earlier, an a-Si film without a pre-existing crystalline interface/seed layer has been observed to crystallize at temperatures above 700℃ [4-2, 3] and due to the use of glass substrate we were not able to exceed this temperature during the annealing process. Thus the maximum temperature was kept at 480℃ and as we expected, no diffraction peak was observed for Si in the sample without the Cu layer (Fig.4.4) meaning that the crystallization of a-Si has not taken place.

Figure 4.5 shows the XRD patterns for the Ta[3 *nm*]/Cu[10 *nm*]/Si[50 *nm*] stack for the four cases of: i) as deposited, ii) annealed to 340℃, iii) annealed to 410℃ and iv) annealed to 480℃. Peaks were indexed according to the Inorganic Crystal Structure Database (ICSD).

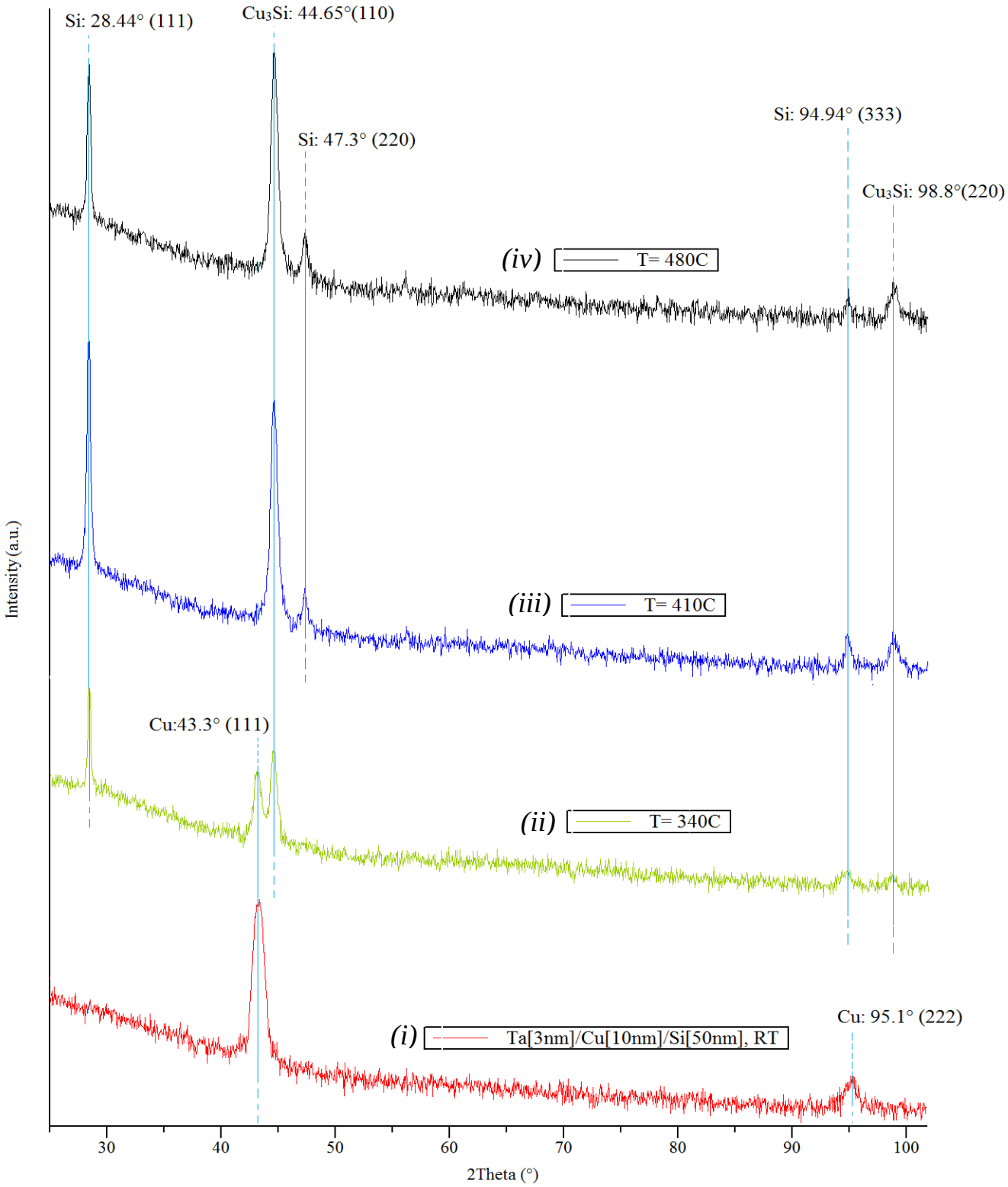

Figure 4.5: The XRD patterns for Ta/Cu/Si stack. *i*) as deposited at room temperature, *ii*) annealed to 340℃, *iii*) annealed to 410℃ *iv*) annealed to 480℃

As can be seen from the diffraction pattern of the as-deposited sample in Fig.4.5, the only observable peaks are located at $2\theta = 43.3°$ and $2\theta = 95.1°$ and they respectively belong to (111) and (222) copper planes which are parallel to the surface of the sample. No silicon peak was observed for this sample.

Copper has a face-centred-cubic (fcc) crystal structure and unlike Si that has an as-deposited amorphous structure, Cu grows along the [111] direction on top of Ta. Figure 4.6 shows the atomic structure of copper. The atoms on the (111) planes of the fcc structure are arranged in a hexagonal pattern.

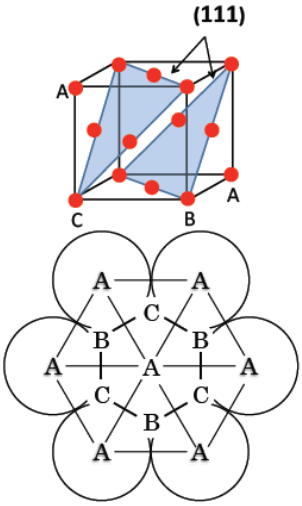

Figure 4.6: A, B, and C are atomic planes. The stacking structure of an fcc lattice viewed from the [111] direction

After annealing the samples with the Cu layer to T=340℃ and higher temperatures, small diffraction peaks start to appear at 2θ = 28.44°, 44.65°, 94.94° and 98.8°. After comparing the results with the powder diffraction patterns for silicon and copper-silicon compounds from the ICSD, the peaks were identified and the results are shown in Table 4.2.

Copper forms several compounds with silicon that are stable at room temperature: Cu_3Si, $Cu_{15}Si_4$ and Cu_5Si. Among these compounds, Cu_3Si is the most Si-rich silicide and was the first and only one that formed during the annealing process. In the annealing temperature range of our experiment, Cu_3Si was the only silicide phase that was identified based on the XRD results.

2θ(°)	28.44	44.65	47.3	94.94	98.8
composition	Si	Cu_3Si	Si	Si	Cu_3Si
hkl plane	(111)	(110)	(220)	(333)	(220)

Table 4.2: Si and Cu_3Si diffraction peak positions and corresponding (hkl) planes

The crystal structure of silicon (diamond cubic) and Cu_3Si (trigonal) are shown in Figure 4.7(a) and (b).

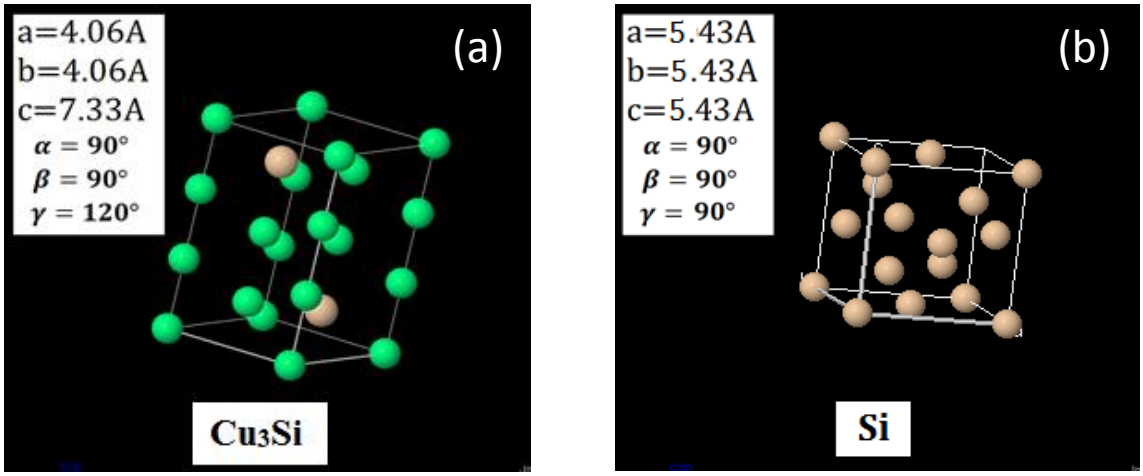

Figure 4.7: Unit cell structures of (a) Cu_3Si and (b) Si crystals from the ICSD

If annealing continues to higher temperatures (Fig.4.5 iii and iv), the Si and Cu_3Si peaks become stronger while the Cu peaks start to diminish as the copper is being consumed to form copper silicide. The XRD results also show that the silicon film has a preferential growth along the [111] direction. By using Scherrer's formula, the grain size of silicon crystallites along this direction can be calculated:

$$grain\ size \sim \frac{0.9\,\lambda}{(FWHM)\cos(2\theta)},$$

where λ is the X-ray's wavelength and 2θ is the Bragg angle. The FWHM of the silicon (111) peak from the $\theta - 2\theta$ scans was measured to be 0.26° for all the annealed

samples (Fig. 4.5 ii, iii and iv). Without considering the instrumental broadening, the lower bound for the size of silicon grains was determined to be $\sim$ 31 *nm*.

Finally, Figure 4.8 shows the omega scan performed on Si (111) peak for the sample that was annealed to 410℃ (Fig.4.5 iii). The FWHM of the silicon peak is 1.11°**.**

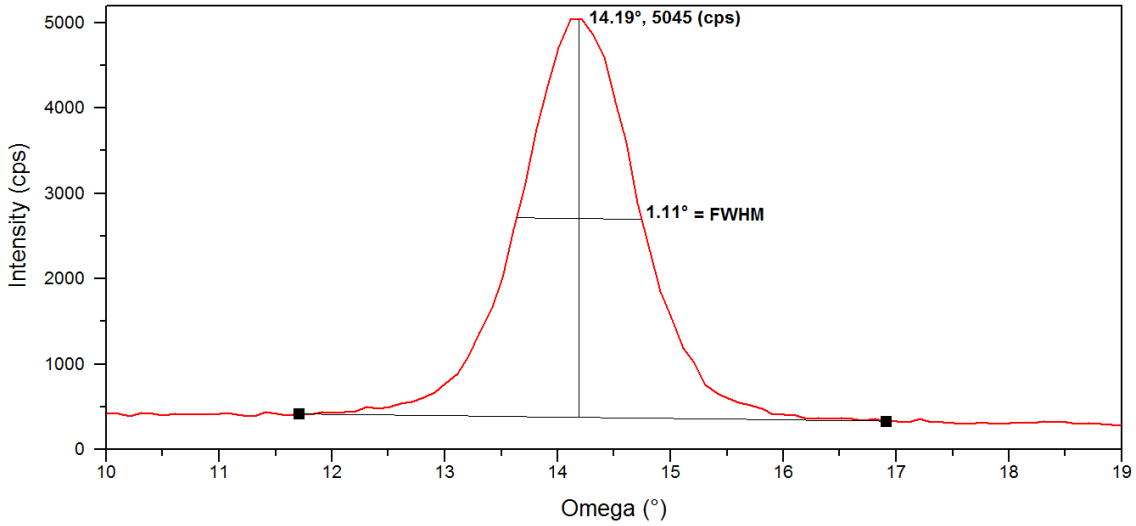

Figure 4.8: The omega scan of the silicon (111) peak from the sample with a copper layer and annealed to 410℃. FWHM of this peak is 1.11°.

It is evident from the diffraction patterns (Fig.4.4 and 4.5) that adding a 10 *nm*-thick layer of copper has reduced the crystallization temperature of Si to at least 340℃. In the next section, the driving force behind the Cu-Si reaction, the phase diagram of the binary system, and the mechanism behind the crystallization of silicon are discussed.

4.4 Discussion

Copper-Silicon System

Copper belongs to the group of 3d transition metals and has an atomic number 29. Silicon is a metalloid with atomic number 14. A Si atom has four valence electrons in the outer orbital and has four nearest neighbors in the crystal lattice. Thus, all outer electrons form four sets of paired stable covalent bonds. Unlike silicon, copper has a

weakly bonded electron in the outer orbital which is responsible for copper's high electrical and thermal conductivity. Some of the atomic and physical properties of copper and silicon are listed in Table 4.3.

	Cu	Si
Atomic Radius (*Å*)	1.35	1.10
Atomic Volume (cm^3/mol)	7.1	12.1
Crystal Structure	Cubic face centered	Cubic face centered
Lattice Constant (*Å*)	3.610	5.431
Electron Configuration	[Ar] $3d^{10}$ $4s^1$	[Ne] $3s^2$ $3p^2$
Atomic Mass (*a.m.u*)	63.546	28.0855
Density (g/cm^3 @ 293 *K*)	8.96	2.33
Electronegativity (*Pauling*)	1.9,1.7	1.8, 1.7
Melting Point (℃)	1085	1414
Thermal Conductivity ($Wm^{-1}k^{-1}$)	401	149
Electrical Conductivity (*S/m* @ 293 *K*)	59.6×10^6	1.56×10^{-3}

Table 4.3: Atomic structure and physical properties of copper and silicon

Copper Diffusivity in Silicon

The weakly bonded single electron in the copper 4s orbital makes Cu one of the fast diffusing elements in silicon [4-19]. Such a configuration allows copper to lose its valence electron and significantly reduce its atomic radius from 1.35 *Å* to ionic radius of 0.77 *Å* [4-20]. Hall and Racette [4-19] and Gallagher [4-22] were the first to show that copper diffuses in silicon as a positively charged ion. Due to the small ionic radius, copper diffuses as an interstitial ion rather than substitutional atom. The intrinsic diffusivity of interstitial copper in silicon is $2.8\times10^{-7}\ cm^2\ s^{-1}$ at 300 *K* and $4.0\times10^{-6}\ cm^2\ s^{-1}$ at 750 *K* [4-23]

which is the maximum annealing temperature. In the presence of acceptor type elements such as elements in the third column of the periodic table, copper diffusivity will be reduced since the positively charged interstitial copper pairs with the negatively charged substitutional acceptor element. The consequence of this pairing is that at any moment only a fraction of copper atoms are mobile and the rest are temporarily trapped [4-19].

Solubility of Copper in Silicon

In contrast to diffusivity, the solid solubility of copper in silicon is insignificant and it dramatically changes at different temperatures. While the solubility of Cu in Si reaches 10^{18} cm^{-3} at 1000°C, at room temperature the solubility drops to less than 1 Cu atom per cm^3 [4-24]. Therefore, all the copper dissolved in the bulk of the silicon during the heat treatment will either precipitate or diffuse out after the annealing process is over.

Figure 4.9 shows the Cu-Si phase diagram. As is shown in the diagram, the solid solubility limit of silicon in copper is much greater than that of copper in silicon. The maximum solid solubility of silicon in copper reaches 11.5 atomic % at 843°C [4-26]. This difference in the extent of solubility limit can be explained by the *relative valence effect* that was first proposed by Hume-Rothery. According to Hume-Rothery, an element with lower valence (copper) is more likely to have a greater solubility for an element with higher valence (silicon) than the opposite case [4-26].

In the case that silicon is the solvent, the bonding is covalent and the eventual substitution of copper in silicon lattice disrupts the covalent sharing of electrons between the Si atom and its 4 nearest Si neighbors. This disruption increases the internal energy and the solubility limit of Cu in Si depends on the extent to which the silicon lattice is able to absorb the increased energy. In the case that copper is the solvent, the bonding type is metallic and the substitution of a copper atom with a silicon atom adds 3 electrons that are not normally present in a lattice composed only of copper. Because of the half-filled valence band of copper, energy states are available and additional valence electrons of silicon can be accommodated. More silicon atoms can be added to the lattice until the Fermi energy level reaches a limiting point and Si concentration at this level determines the limit of solubility [4-26].

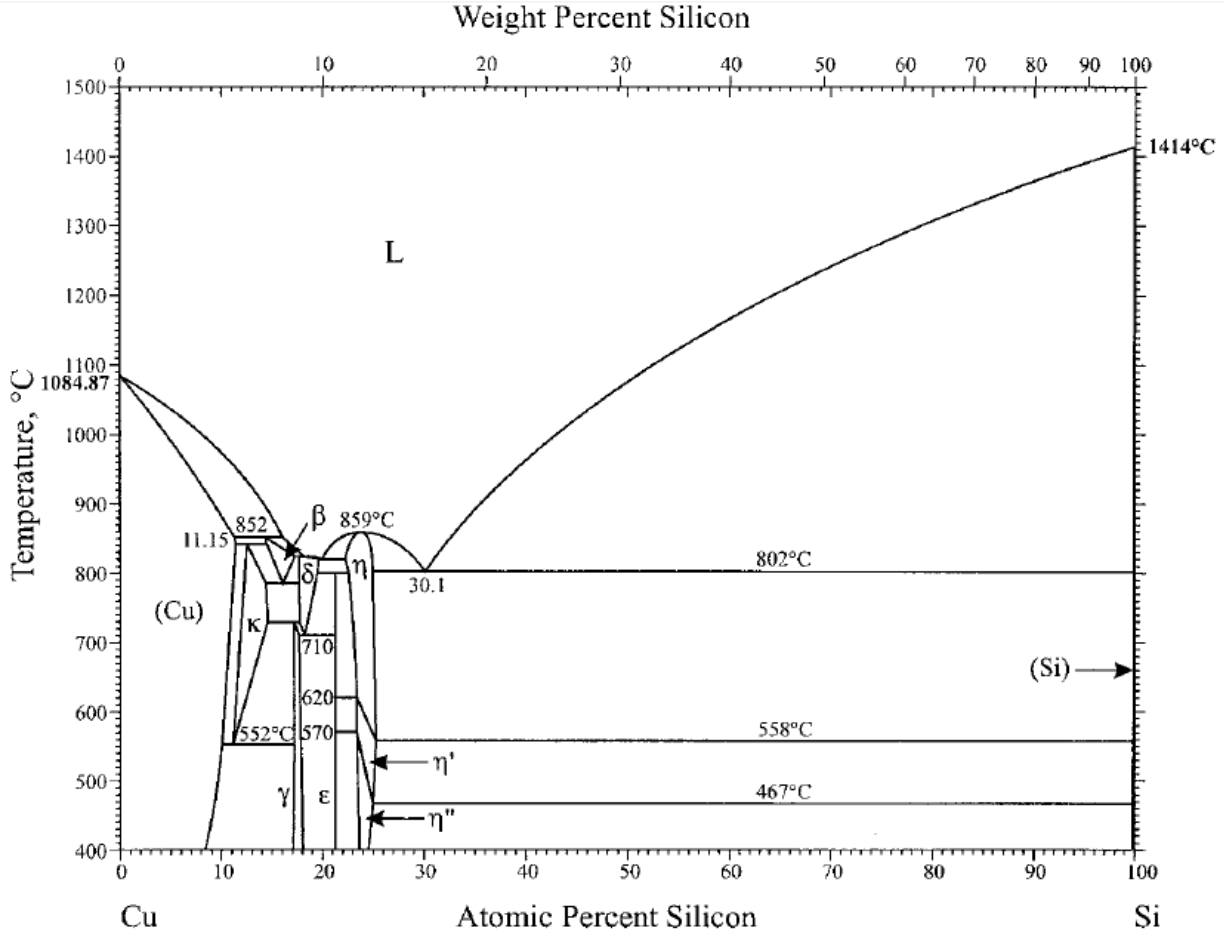

Figure 4.9: Cu–Si phase diagram assessed by Olesinski and Abbaschian [4-25]

Intermetallics

The Cu-Si phase diagram contains eight intermetallic compounds, three of which are stable phases at room temperatures:η''(Cu_3Si), ε($Cu_{15}Si_4$) and γ(Cu_5Si). The total stoichiometric range for these three compounds is rather narrow (8 atomic %). Cu_3Si has two high temperature modifications which are indicated with η and η' in the phase diagram. Cu_3Si- η'' is the most commonly observed phase in Cu-Si systems [4-27]. As can be seen from the phase diagram the transition temperature for the Cu_3Si polymorphs strongly depends on the composition.

After comparing the XRD data of our samples with the powder diffraction patterns of copper-silicon compounds in the ICSD, Cu_3Si- η'' was the only copper-silicide compound that was identified in our samples during the heat treatment. There have been numerous

crystallographic reports on the crystal structure of Cu_3Si- η'' [4-27, 28], however, based on the ICSD, the crystal structure of the Cu_3Si- η'' phase is trigonal and the diffraction peak positions of the Cu_3Si- η'' in our samples shows that the copper-silicide η'' phase grows in [110] direction. Two of the most recognized works on the crystal structure of Cu_3Si- η'' are by Solberg [4-28] and Mukherje *et al.*[4-29] . Solberg investigated the crystal structure of Cu_3Si- η'' precipitates by means of transmission electron microscopy and proposed an orthorhombic crystal lattice and Mukherje *et al*. concluded that the crystal structure of Cu_3Si- η'' is tetragonal.

Figure 4.10 shows the atoms arrangements in the crystallographic planes of Si, Cu and Cu_3Si- η'' that are responsible for the diffraction peaks.

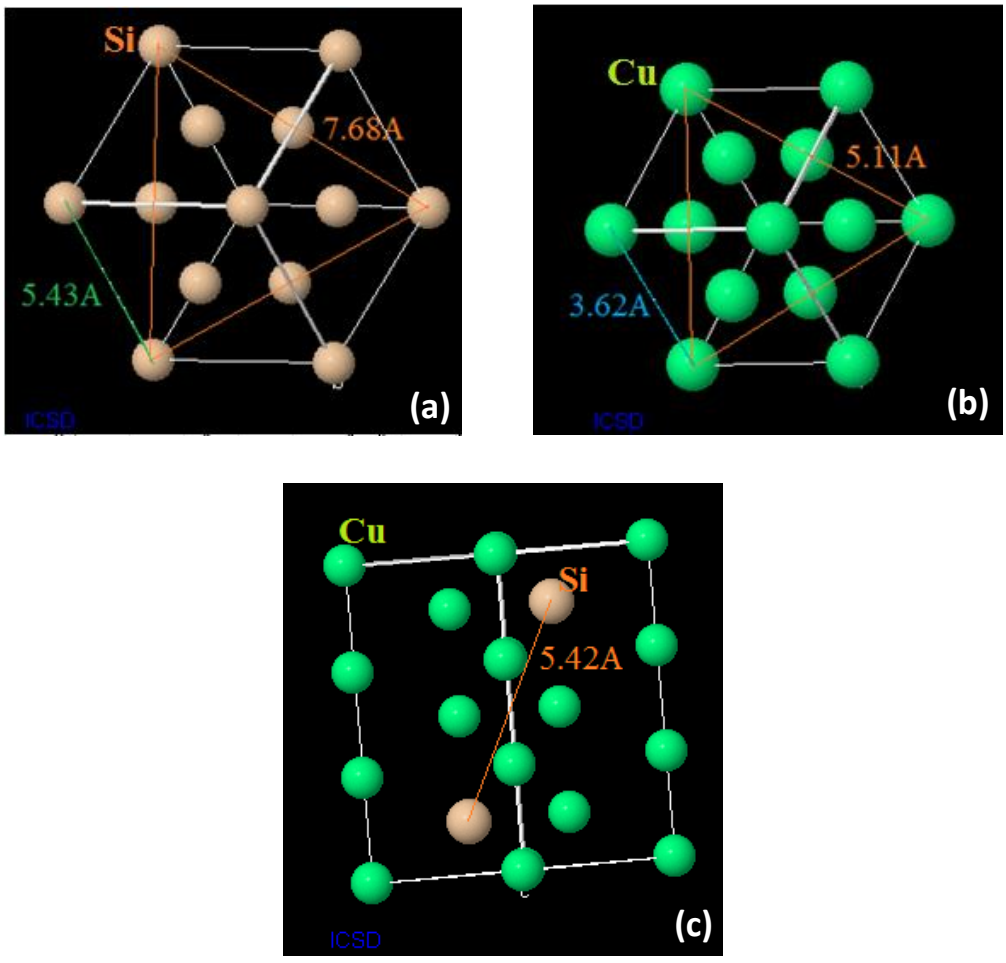

Figure 4.10: The atomic arrangements in the crystallographic planes of: (a) Silicon (111) plane, (b) Copper (111) plane, and (c) Cu_3Si (110) plane

Crystallization Kinetics of a-Si/Cu Bilayer under Thermal Annealing

There are numerous studies that show for the silicide forming metals, the formation of silicide enhances the crystallization of silicon. However, the proposed crystallization mechanism is different for various silicide-forming metals.

There are reports that the transition metals such as Ni and Pd enhance Si crystallization by the epitaxial growth of c-Si on the forming silicides [4-30, 31]. Unlike Ni and Pd, Cu appears to enhance crystallization by a different mechanism.

Up to now, the most widely accepted mechanism for Cu-induced crystallization of silicon is that upon annealing the Cu-Si bilayer, Cu diffuses into amorphous silicon and reacts with Si and forms Cu_3Si. Cu is the dominant diffusing species in the formation of Cu_3Si [4-32]. The Cu_3Si precipitates then serve as the nucleation sites and the latent heat released during the formation of copper silicide facilitates the phase transition from a-Si to poly-Si [4-9].

Ward *et al*. and Becht *et al*. showed that copper diffusion is a limiting factor in the growth of Cu_3Si in bulk samples. It has been shown that for temperatures below 475℃, the grain boundary diffusion of Cu is the controlling mechanism in Cu_3Si formation and at higher temperatures, bulk diffusion becomes dominant [4-33, 34].

In all the literature that I have reviewed ([4-35, 37]) on Cu induced crystallization of Si, silicon is preferentially grown in the [111] direction. However, in contrast to the other silicide-forming transition metals, such as Ni and Pd, there is no report on the epitaxial growth of Si on Cu_3Si nuclei. Among all the papers, only one suggested what may have caused the preferential growth. Lee *et al.* proposed that the [111] growth direction of silicon may be due to the anisotropic properties of c-Si [4-14]. The region surrounding the a-Si/c-Si interface is strained due to the different structures and densities. The strain energy arising from the situation can be anisotropic because of the anisotropic elastic properties of c-Si. For Si, the <111> directions have the highest strain energy density which indicates that a-Si contacting the [111]-oriented c-Si receive the highest strain energy density along the growth direction and they are likely to undergo crystallization in that direction with the highest rate.

Although Cu_3Si was the only copper silicide observed in our samples, there are reports that by prolonging the annealing process, increasing the annealing temperature, and having the right Cu-Si ratio other stable silicon-copper compounds will be formed by subsequent reactions between copper and Cu_3Si [4-38].

4.5 Conclusion

I have studied the effect of Cu on the crystallization temperature of a-Si under thermal annealing. A bilayer of a-Si[50 *nm*]/Cu[10 *nm*] was deposited on Ta-covered glass substrates and annealed to different temperatures (340℃-480℃) for 20 minutes. The crystallization behaviour of the samples was examined by using the XRD measurement. It is confirmed that inserting a layer of Cu can effectively reduce the crystallization temperature of a-Si.

Under thermal annealing the formation of Cu_3Si and poly-Si was observed. The results show that Cu_3Si is the dominant copper silicide phase at the operating temperatures and Si crystallites grow preferentially in the [111] direction.

References

[4-1] W. Knaepen , C. Detavernier, R.L. Van Meirhaeghe, J. Jordan Sweet, C. Lavoie, *In-situ X-ray Diffraction study of Metal Induced Crystallization of amorphous silicon*, Thin Solid Films 516 4946-4952 (2008).

[4-2] G. Farhi, M. Aoucher, T. Mohammed-Brahim, *Study of the solid phase crystallization behavior of amorphous sputtered silicon by X-ray diffraction and electrical measurements*, Sol. Energy Mater. Sol.Cells 72, 551-558 (2002).

[4-3] J. A. Olson and G. L. Roth, *Kinetics of solid phase crystallization in amorphous silicon*, Mater. Res. Sci. Symp. 74, 319 (1987).

[4-4] L. Csepregi, J. W. Mayer, and T. W. Sigmon, Phys. Lett. A 54, 157 (1975).

[4-5] M. Miyasaka and J. Stoemenos*, Excimer Laser Annealing of amorphous and Solid-Phase-Crystallized Silicon films*, J. Appl. Phys. 86, 5556 (1999).

[4-6] Y. Z. Wang and O. O. Awadelkarim, Appl. Phys. A: Mater. Sci. Process.70, 587 (2000).

[4-7] W. Knaepen, C. Detavernier, R.L. Van Meirhaeghe, J. Jordan Sweet , C. Lavoie, *In-situ X-ray Diffraction study of Metal Induced Crystallization of amorphous silicon*, Thin Solid Films 516 4946–4952 (2008).

[4-8] Y. Liu, S. Song, D. Mao, H. Ling, M. Li, Microelectronic Engineering 75(3) 309-315 (2004).

[4-9] Yung-Chiun Her, Chih-Wei Chen, and Chun-Lin Wu, J. Appl. Phys. 99, 113512 (2006).

[4-10] Seung-Ik Jun, Philip D. Racka, Timothy E. McKnight, Anatoli V. Melechko, and Michael L. Simpson, Appl. Phys. Lett. 89, 022104 (2006).

[4-11] Wei-Chieh Hsueh and Si-Chen Lee, Fellow, IEEE, IEEE TRANSACTIONS ON ELECTRON DEVICES, Vol. 50, March 2003.

[4-12] G. A. Bhat, Z. H. Jin, H. S. Kwok, and M. Wong, *The Effects of the MILC/MIC Interface on the Performance of MILC-TFTs*, in 56th Device Research Conference Digest, Charlottesville, VA, pp. 110–111, June 1998.

[4-13] S. H. Park, S. I. Jun, K. S. Song, C. K. Kim, and D. K. Choi, Jpn. J. Appl. Phys. 38, L108 (1999).

[4-14] Sung Bo Lee, Duck-Kyun Choi, and Dong Nyung Lee, *Transmission electron microscopy observations of Cu-induced directional crystallization of amorphous silicon*, J. Appl. Phys. 98, 114911 (2005).

[4-15] Nast O and Wenham SR. J Appl Phys; 88(1):124 (2000).

[4-16] Soo Young Yoon, Seong Jin Park, Kyung Ho Kim, Jin Jang, Thin Solid Films 383 34-38 (2001).

[4-17] Jong Hyun Choi, Do Young Kim, Seung Soo Kim, Seong Jin Park, Jin Jang, Thin Solid Films 440 1–4 (2003).

[4-18] M. Zou, L. Cai, H. Wang, W. Brown, Mater. Lett. 60, 1379 (2006).

[4-19] Andrei A. Istratova and Eicke R. Weber, Journal of The Electrochemical Society, 149 (1) G21-G30 (2002).

[4-20] B. Bosacchi and P. Franzosi, *The Electron-Phonon Enhancement Factor on Fermi Surface of Copper*. Phys. Stat. Sol. (b) 77:457 (1976).

[4-21] R.H. Hall and J.H. Racette, J. Appl. Phys. 35, 379 (1964).

[4-22] C.J. Gallagher, J. Phys. Chem. Solids 3, 82 (1957).

[4-23] A. Istratov, C. Flink, H. Hieslmair, E. Weber, T. Heiser, *Intrinsic Diffusion Coefficient of Interstitial Copper in Silicon*. Phys. Rev. Lett. 81:1243 (1998).

[4-24] K. Graff, *Metal Impurities in Silicon-Device Fabrication*, Springer, Berlin (1995).

[4-25] R.W. Olesinski and G.J. Abbaschian, *Bull. Alloy Phase Diagrams*, *7*(2), pp. 170-78 (1986).

[4-26] Daniel D. Pollock*, Physical Properties of Materials For Engineers,* 2nd Edition, CRC Press (1993).

[4-27] G. Weber, B. Gillot and P. Barret, Phys. Stat. Sol. A 75 567 (1983).

[4-28] J.K. Solberg, *Crystal-Structure of Eta-Cu3Si Precipitates in Silicon*, Acta Crystallogr., Sect. A: Found. Crystallogr., 34, 684-698 (1978).

[4-29] K.P. Mukherje, J.P. Bandyopadhyaya, K.P. Gupta, *Phase Relationship and Crystal Structure of Intermediate Phases in Cu-Si System in Composition Range of 17 at Pct Si to 25 at Pct Si*, Trans. Metall. Soc. AIME, 245, 2335-2338 (1969).

[4-30] S. W. Lee, Y. C. Jeon, and S. K. Joo, Appl. Phys. Lett. 66, 1671 (1995).

[4-31] C. Hayzelden, J. L. Batstone, and R. C. Cammarata, Appl. Phys. Lett. 60, 225 (1992).

[4-32] L. Stolt and F. M. d'Heurle, Thin Solid Films 189, 269 (1990).

[4-33] W. J. Ward and K. M. Carroll, J. Electrochem. Soc. 129, 227 (1982).

[4-34] J. G. M. Becht, F. J. J. van Loo, and R. Metselaar, Reactivity of Solids 6, 45 (1988).

[4-35] Sung Bo Lee, Duck-Kyun Choi, Fritz Phillipp, Kyung-Sook Jeon, and Chang Kyung Kim*, In situ high-resolution transmission electron microscopy study of interfacial reactions of Cu thin films on amorphous silicon*, Applied Physics Letters 88, 083117 (2006).

[4-36] Y. C. Her and C. L. Wu, J. Appl. Phys. 96, 5563 (2004).

[4-37] Yong Zhao, Jian Wang, Qiang Hu, Dejie Li, *Crystallization of sputtered amorphous silicon induced by silver–copper alloy with high crystalline volume ratio*, Journal of Crystal Growth 312, 3599–3602 (2010).

[4-38] Stella Q. Hong, Craig M. Comrie, Stephen W. Russell, and James W. Mayer, J. Appl. Phys. 70 (7), October 1991.

Chapter 5

Conclusion

The aim of this thesis was to study the fundamental concepts of sputtering, apply this technique for film deposition, and investigate two of the most important properties of the thin films: film uniformity and crystal structure. The important contributions from this work are listed below.

5.1 A Model for Film Thickness Distribution

The control of film thickness during the thin films fabrication process is of crucial importance. In this thesis, a simulation model was developed to predict the thickness distribution of the films deposited by means of magnetron sputtering technique. The most challenging part in developing the model was to determine the angular distribution of the sputtered particles. Generally, in sputtering, the angular distribution of particles follows a variation of the cosine distribution (cosine, under-cosine, over-cosine or heart-shaped) depending on the energy of the bombarding ions. It has been shown that for the case of magnetron sputtering the angular distribution of sputtered particles is that of a heart-shaped. So the heart-shaped distribution was employed to represent the angular distribution of sputtered particles in our experiment. To verify the model, several silicon films were deposited at different source-substrate distances and their thicknesses were measure by X-ray reflectometry measurements. Good correlation was demonstrated between the simulations and experimental results meaning that the choice of the hear-

shaped angular distribution was valid. It is expected that the model can be used to predict an optimum source-substrate geometry that results in a uniform film deposition for future projects.

5.2 Copper-Induced Crystallization of Silicon

Polycrystalline silicon thin films are a crucial part of many technological areas such as semiconductor, microelectronics and solar industries. Metal induced crystallization (MIC) of silicon is one of the cost-effective and low temperature methods to fabricate poly-Si thin films. In this thesis, silicon films were sputter-deposited in contact with a copper layer and annealed to high temperatures to perform the induced crystallization. The microstructural changes of silicon films were then examined by X-ray diffraction measurements. The crystallization of silicon was observed at 340℃ which is considerably lower than the crystallization temperature of silicon without any crystalline interface (~ 700℃). The X-ray diffraction results also show that silicon crystallizes in a preferential [111] direction that could be attributed to the anisotropic mechanical properties of silicon. The FWHM of the omega scan for the (111) peak of silicon was found to be 1.11° which is an indication of the good degree of crystallinity along the [111] direction.